Inclusion of DLVO forces in simulations of non-Brownian solid suspensions
Rheology and structure

Srinivasan, Sudharsan; Van den Akker, Harry E.A.; Shardt, Orest

DOI
10.1016/j.ijmultiphaseflow.2021.103929

Publication date
2022

Document Version
Final published version

Published in
International Journal of Multiphase Flow

Citation (APA)
Srinivasan, S., Van den Akker, H. E. A., & Shardt, O. (2022). Inclusion of DLVO forces in simulations of non-Brownian solid suspensions: Rheology and structure. *International Journal of Multiphase Flow*, *149*, Article 103929. https://doi.org/10.1016/j.ijmultiphaseflow.2021.103929

International Journal of Multiphase Flow 149 (2022) 103929

Contents lists available at ScienceDirect

International Journal of Multiphase Flow

journal homepage: www.elsevier.com/locate/ijmulflow

Inclusion of DLVO forces in simulations of non-Brownian solid suspensions: Rheology and structure

Sudharsan Srinivasan [a,b,*], Harry E.A. Van den Akker [a,b,c], Orest Shardt [a,b,*]

[a] Synthesis and Solid State Pharmaceutical Centre (SSPC), University of Limerick, V94 T9PX, Limerick, Ireland
[b] Bernal Institute and School of Engineering, University of Limerick, V94 T9PX, Limerick, Ireland
[c] Transport Phenomena Lab, Department of Chemical Engineering, Delft University of Technology, Van der Maasweg 9, 2629 HZ Delft, The Netherlands

ARTICLE INFO

Keywords:
Rheology
Suspensions
Aqueous electrolyte
Lubrication corrections
DLVO forces
Immersed boundary-Lattice Boltzmann method

ABSTRACT

The understanding of the rheological behaviour of suspensions in aqueous electrolytes is necessary for the optimal design of hydraulic transport lines. In these applications, particle size is at least 10 micron, and the particle Reynolds number, Re_p, is finite: $O(10^{-1})$. Although there are some experimental and numerical data on the rheology of such suspensions, the number of detailed analyses is limited. Therefore, 3-D direct numerical simulations of dense suspensions in aqueous electrolytes are conducted to assess the dynamics of the relative apparent viscosity and particle structures. The solid–liquid interfaces are resolved, and the flow is simulated, employing an *in-house* immersed boundary-lattice Boltzmann method code. In addition to the hydrodynamics resolved in the computational grid, our simulations include unresolved sub-grid scale lubrication corrections and non-contact electric double layer (EDL) and Van der Waals forces for a wide range of particle volume fractions, ϕ_v, at a single $Re_p = 0.1$. Under these conditions, the contribution of the Van der Waals force was found to be weak. With an increase in ϕ_v, the effect of EDL forces decreased the relative apparent viscosity. Particle layering and structural arrangements were analysed for $\phi_v = 43$ and 52%. As the Debye length (i.e., the thickness of EDL) decreases, the particle layers near the walls weakened. The analyses reveal how at these high volume fractions, chain-like assemblies are transformed into hexagonal arrangements.

1. Introduction

This paper presents an extension of an Immersed Boundary (IB) Lattice Boltzmann (LB) technique for assessing the rheology of a suspension (Srinivasan et al., 2020a) to the cases of suspensions consisting of particles with electrically charged surfaces such as food matrices (Silaghi et al., 2010), Portland cement (Ferrari et al., 2011), waste-water sludge (Liu et al., 2012), and drilling mud (Hamed and Belhadri, 2009). In such applications, both the attractive Van der Waals forces and repulsive electrostatic forces may play a distinctive role not considered in earlier work. These forces may have an impact on the structures of particles in a flowing suspension and consequently on the rheology as expressed in terms of a relative apparent viscosity. We restrict ourselves to non-Brownian particles of order 100 μm and to finite particle Reynolds number of order 10^{-1}. The resulting resolved simulations will provide an 'inner' view of the complex response of multiple charged particle assemblies subjected to shear. The viscosity of particularly more concentrated suspensions strongly depends on the dynamics of clusters which may be affected by the charges on the particle surfaces (Lattuada et al., 2016). Besides, the insights acquired via these simulations may be useful for studies on shear assisted agglomeration (Mumtaz et al., 1997; Hollander et al., 2001).

The flow characteristics of charged particles are affected by both hydrodynamic forces and non-hydrodynamic interactions as described by the Derjaguin–Landau–Verwey–Overbeek (DLVO) theory (Masliyah and Bhattacharjee, 2006; Berg, 2010). Non-DLVO molecular forces being ignored, such as those between particles with a soft coating (Karan et al., 2020), the focus is on two types of short-range interactions that are not being resolved on the LB lattice, viz. hydrodynamic lubrication corrections (Nguyen and Ladd, 2002; Derksen and Sundaresan, 2007) and non-hydrodynamic DLVO interactions. We study their effects on the rheology over a broad range of solid volume fractions. Furthermore, the assumption is that the surfaces of the spheres are perfectly smooth, and therefore, frictional contact forces (Toll and Månson, 1994) are not considered when modelling sub-lattice scale interactions.

According to the classical DLVO theory, the particles get attracted or repelled depending on their surface charge and on the distribution of ions in solution (Masliyah and Bhattacharjee, 2006). The counter-ions

---

[*] Corresponding authors.
E-mail addresses: sudharsansrinivasan1992@gmail.com (S. Srinivasan), Harry.VanDenAkker@ul.ie (H.E.A. Van den Akker), Orest.Shardt@ul.ie (O. Shardt).

https://doi.org/10.1016/j.ijmultiphaseflow.2021.103929
Received 15 April 2021; Received in revised form 28 September 2021; Accepted 5 December 2021

in the liquid are attracted to the surface charges and form a diffuse Electric Double Layer (EDL), the thickness of which is characterised by the Debye length. When the EDLs of two (or more) like-charged particles overlap (Berg, 2010), the effect is a repulsive force. The net charge within the double layer is opposite to that of the surface and decays with increasing distance from the surface. With decreasing ion concentration, the EDL thickens (Berg, 2010; Pednekar et al., 2017). This allows the repulsive EDL interactions to dominate over the attractive Van der Waals forces.

Over the last two decades, several attempts have been made to interpret the physics of suspensions with electric charges via experimental (Chaouche and Koch, 2001; Hermes et al., 2016; Lattuada et al., 2016; Vázquez-Quesada et al., 2017) and numerical approaches (Rouyer et al., 2000; Sierou and Brady, 2002; Kromkamp et al., 2005; Yeo and Maxey, 2010; Andreotti et al., 2012; Gallier et al., 2016; McCullough et al., 2021). Most papers in the literature consider the dependence of the rheology on hydrodynamic and other contact force (frictional) models. The effects due to surface potentials (especially the contributions from the close-range Van der Waals and EDL forces) are often ignored when simulating suspensions in aqueous electrolytes. In this paper, we demonstrate the effects of including DLVO forces in computational studies of the suspension structure and rheology of micron-sized particles.

Some recent advances in learning about the importance of including these short-range DLVO forces have been made possible via theory (Karan et al., 2020) and simulations (Lin et al., 2015; Mitchell and Leonardi, 2016; Sarkar et al., 2017; Wang et al., 2019; Vowinckel et al., 2019; Hayakawa, 2020). Pednekar et al. (2017) used the Discrete Element Method (DEM) with Lubrication Flow (LF) to simulate colloidal Brownian suspensions with attractive forces. Their emphasis was on investigating the effect of different strengths attractive forces on the apparent viscosities and contact networks. They found that the impact of attractive forces leads to an increased viscosity at low shear rates and the viscosity decreases gradually to a plateau at high shear rates. Mari et al. (2014) included EDL forces in their simulations and showed the Discontinuous Shear-Thickening (DS-T) rheology of suspensions with solids fractions between 45 and 56%. It may be necessary to note that these simulations were performed under zero Reynolds number (Stokes flow) conditions. To the best of our knowledge, the literature on suspension behaviour with finite inertia under the influence of surface forces is limited.

Recently, we have developed computer codes to simulate dense solid–liquid suspensions using an IB-LB model (Srinivasan et al., 2020a, 2021). One of the benefits of conducting simulations is that they allow us to investigate details, for example, by monitoring the particle rotation rates in a suspension (Srinivasan et al., 2020a), that may not be possible through experiments. We now modify the sub-lattice scale forces to include the contribution of unresolved lubrication correction and DLVO forces and demonstrate the effects of Debye length on cluster structures and relative viscosities.

The purpose of this study is to develop an understanding of the resolved three-dimensional simulations of solid–liquid suspensions in aqueous electrolytes that undergo deformations due to simple shear flow. The effects of changes in the inter-particle collision schemes on the relative viscosity and cluster structure are the outcomes of our research. The simulations mimic the suspension behaviour in a rheometer, where particles of order 150 μm in radius are sheared between parallel plates separated by a 2 mm gap. The confinement ratio $\delta = 2R/H = 0.15$ (where R is the particle radius and H is the gap between the parallel plates), which we match in our simulations. This paper is a next step in developing a code to mimic suspensions under time-varying shear rates with DLVO forces, with the end goal that we can improve our understanding of the transient response of suspensions to hydraulic transport conditions.

This paper is arranged as follows: first, in Section 2, we describe our numerical IB-LB approach to simulate suspension flows. Since a detailed description of the simulation methods is given in Srinivasan et al. (2020a), here, we present just a brief summary of the method. Also the modelling equations of DLVO theory, values of lubrication cutoffs, integration of particle motion, and a brief description of our simulation cases are given in this section. Section 3 details the effect of including DLVO forces on collision between two particles by comparing the simulation results with our previous findings. In Sections 4.1 and 4.2.1, we discuss the time-evolution of apparent viscosities and cluster structures of dense suspensions for varying strengths of EDL forces. In Section 4.2.2, we present a qualitative and quantitative analysis of the structuring and ordering of particles, also by comparing our simulations with literature data. Finally, in Section 5, we provide our concluding remarks.

2. Simulation methods

2.1. Flow solver and boundary conditions

The flow of the incompressible Navier–Stokes equations is solved by using the lattice Boltzmann method (Chen and Doolen, 1998) with the BGK collision operator. In this method, the continuous Boltzmann equation is discretised up to second order in space, momentum, and time using the finite difference scheme. The simulations are three-dimensional, and the LB populations move with discrete velocities on a regular Cartesian grid represented by a $D3Q19$ lattice model. The no-slip condition at the surface of each particle is enforced by adopting Feng and Michaelides (2004) immersed boundary method. The surfaces of the particles are represented by a set of equally spaced Lagrangian points called marker and reference. The marker points get advected during the simulation, and any small displacement in the position of these points leads to a significant force called the Lagrangian force. These local forces which are present only on the surface of each particle can be interpreted as a distribution of hydrodynamic forces. Through a linear interpolation scheme (Krüger et al., 2017; Srinivasan et al., 2020a), we spread these local forces to the adjacent fluid nodes using the Shan and Chen (1993) forcing scheme to compute the body force density. The velocity of each marker point is interpolated back from the adjacent fluid velocities, and the new marker positions are computed using an explicit Euler integration. The reference points are updated each time step by tracking the small-angle rotation of all particles (Srinivasan et al., 2020a). In addition to employing a no-slip condition at the surface of each particle, Ladd (1994a) and Ladd (1994b) bounce-back scheme with momentum correction was used to enforce the no-slip condition for the sliding plates on the top and bottom (Srinivasan et al., 2020a).

2.2. Sub-lattice scale modelling

We need to consider the sub-lattice contribution of fluid–particle interactions because particles with their variable advection and rotation rates may approach each other, certainly during collisions, at distances smaller than the lattice spacing used in the simulation. Both the interstitial fluid flows and the positions and motions of the particles, therefore, require modelling of these sub-lattice corrections to forces and torques to capture the effects of the unresolved flow field during collision process. In this paper, we include the corrections of lubrication forces and torques, as well as the DLVO-based attractive Van der Waals forces and repulsive forces due to surface charges.

2.2.1. Lubrication correction: forces and torques

Detailed modelling expressions and benchmark simulations of lubrication forces and torques are provided in Appendix. When implementing these corrections in the IB-LB code, we only added the difference between the under-resolved LB values and the analytical terms. For large interparticle gaps, the hydrodynamic forces and torques are accurately evaluated by the LB simulation. However, in the case of small interparticle gaps, the cutoff to turn on the Lubrication Correction (referred as LC from now onward) is chosen such that we restore the correct behaviour of the forces and torques on the particle. The forces calculated for the intermediate gap sizes are not necessarily accurate — although they do interpolate reasonably between the two extremes. While the specifics of how these cutoffs are chosen are given in Appendix, the values of h_o^n/R_{hyd}, h_o^t/R_{hyd}, and h_o^r/R_{hyd} (where h_o^n, h_o^t, h_o^r, and R_{hyd} are the normal, tangential translational and rotational lubrication cutoffs, and the hydrodynamic radius, respectively) are 0.5, 0.1, and 0.01, respectively. We use these values in suspension simulations to account for the unresolved details of the flow between the neighbouring particles. For particle–wall interactions, we turn on the LC when the gap between any particle and either wall is less than $0.01R_{hyd}$.

2.2.2. DLVO forces

A Van der Waals form of force is used to model the attraction between particles when the charged surfaces of two spheres approach each other according to

$$\mathbf{F}_p^a = \frac{A_H R_{hyd}}{12}\frac{1}{h^2}\,\mathbf{n}_{pq}. \tag{1}$$

The superscript a denotes attraction, the parameter A_H (Hamaker constant) is the strength of the attractive force, h is the gap between the spheres, and $\mathbf{n}_{pq} = \dfrac{\mathbf{x}_q - \mathbf{x}_p}{\|\mathbf{x}_q - \mathbf{x}_p\|}$ is the unit vector from sphere p to q (where $\mathbf{x}_p$ and $\mathbf{x}_q$ are the centres of mass of spheres p and q, respectively). The solid back lines in the left panel of Fig. 1 presents the evolution of attractive force as a function of gap size for two different particles with physical radii R_p of 10 and 150 μm, respectively.

These Van der Waals attractive forces compete with the electrostatic repulsive component according to

$$\begin{aligned}\mathbf{F}_p^r &= -\frac{64\pi\eta_\infty k_B T\gamma_\delta^2 R_{hyd}}{\kappa}\exp(-\kappa h)\,\mathbf{n}_{pq}\\ \gamma_\delta^2 &= \tanh^2\left(\frac{ze\psi_\delta}{4k_B T}\right)\end{aligned} \tag{2}$$

where the superscript r denotes repulsion. The variables η_∞, k_B, and T are the number density of the ions, Boltzmann constant, and absolute temperature, respectively. $\kappa^{-1} = \sqrt{\dfrac{\epsilon k_B T}{2z^2e^2\eta_\infty}}$ is the Debye length, where ϵ is the dielectric permittivity of solvent (e.g., water), Z is the valance of ions, $e = 1.6\times10^{-19}$ C is the fundamental charge, and ψ_δ is the zeta potential. At room temperature (20 °C), for water, the Debye length can be written as $\kappa^{-1}(\text{nm}) = \dfrac{0.304}{Z\sqrt{I}}$ (Masliyah and Bhattacharjee, 2006).

In the current manuscript, we present simulations of two scenarios. The first is suspensions without EDL forces ($\psi_\delta = 0$). The second scenario is suspensions with a high zeta potential $\psi_\delta > 175$ mV ($\gamma_\delta^2 > 0.9$), which demonstrates behaviour in the limit $\gamma_\delta^2 \to 1$. The suspension we are interested to mimic is comprised of iron oxide particles suspended in an aqueous carrier liquid with a zeta potential that ranges between −30 mV and +30 mV for pH ranging from 4 to 11 (Liu et al., 2013) for which $0 \le \gamma_\delta^2 \lessapprox 0.1$ is valid. The investigation of suspension rheology under these conditions is not addressed in this paper; nevertheless, the reported data provide a range of suspension viscosities that can be used in future studies.

In Fig. 1*a*, along with the Van der Waals line, the dashed lines represent the contributions of the electrostatic force for varying I (pH) and R_p. In Fig. 1*b*, the total interaction force (i.e. the sum of Van der Waals and EDL) in the physical units is shown. One can see that the EDL forces are approaching constant value over small gaps, while the Van der Waals force is infinite at zero separation. In Fig. 1*c*, the total particle–particle DLVO forces are expressed in LB units; for a symmetric electrolyte solution (e.g. sodium hydroxide, where the anion and cation charges are equal). In all panels, three pH values (10, 11, and 12) are considered to show its effect on the force; however, in the remainder of this paper we consider pH = 11. In order to mimic suspensions with a physical radius of 10 and 150 μm, in simulations, we keep the particle resolution at 8 lu while rescaling all other parameters as given in Table 1.

Following Masliyah and Bhattacharjee (2006), the equations of Van der Waals and EDL interaction of the particle p with either wall are given as

$$\begin{aligned}\mathbf{F}_p^{a-w} &= \frac{A_H R_{hyd}}{6}\frac{1}{h^2}\,\mathbf{n}_{pw}\\ \mathbf{F}_p^{r-w} &= -\frac{128\pi\eta_\infty k_B T\gamma_\delta^2 R_{hyd}}{\kappa}\exp(-\kappa h)\,\mathbf{n}_{pw}\end{aligned} \tag{3}$$

where w represents a wall. Adding these wall contributions to Eqs. (1) and (2), we get the total DLVO force as

$$\mathbf{F}_p^{DLVO} = \mathbf{F}_p^a + \mathbf{F}_p^r + \mathbf{F}_p^{a-w} + \mathbf{F}_p^{r-w}. \tag{4}$$

2.3. Particle motion

In addition to the advection of the marker points, each particle has contributions from its translational $\mathbf{u}_p$ and rotational $\boldsymbol{\omega}_p$ motions. In order to avoid instabilities due to numerical integration, multiple sub-timesteps n_{tp} were used for the integration of particle motion. At the beginning of every sub-time step loop, we first compute the sub-lattice scale forces and torques. Then the spheres' linear motion and positions are updated as

$$\begin{aligned}\mathbf{u}_p^{\langle\delta t+1\rangle} &= \mathbf{u}_p^{\langle\delta t\rangle} + \left(\mathbf{F}_p^{LB} + \mathbf{F}_p^{DLVO} + \mathbf{F}_p^{lub}\right)\frac{\delta t}{M}\\ \mathbf{x}_p^{\langle\delta t+1\rangle} &= \mathbf{x}_p^{\langle\delta t\rangle} + \mathbf{u}_p\delta t\end{aligned} \tag{5}$$

where M is the mass of the sphere, $\mathbf{F}_p^{LB}$ is the resolved (LB) fluid force that arises from the IB method (Srinivasan et al., 2020a), and $\mathbf{F}_p^{lub}$ is the total lubrication force (see Appendix). The time step for particle integration is $\delta t = 1/n_{tp}$. We assume that the DLVO forces do not affect the rotation rates of the particle, and therefore the angular motion is computed from the LB (Srinivasan et al., 2020a) and LC torques (see Appendix) as

$$\boldsymbol{\omega}_p^{\langle\delta t+1\rangle} = \boldsymbol{\omega}_p^{\langle\delta t\rangle} + \left(\mathbf{T}_p^{LB} + \mathbf{T}_p^{lub}\right)\frac{\delta t}{I} \tag{6}$$

where I and $\mathbf{T}_p^{LB}$, and $\mathbf{T}_p^{lub}$ are the moment of inertia of the spheres, LB torques, and lubrication torques (see Appendix), respectively.

When simulating suspension flows, the particles may occupy a significant volume of the simulation box (for example, ϕ_v up to 52% – highest solids concentration considered in this paper), and therefore the number of collisions between spheres increases substantially that – in turn – increases the simulation wall time. Therefore, to speed up the calculations of these interparticle interactions, we implemented a binning algorithm that identifies particles with specified distances from each other. For more information about such binning algorithms, see e.g. Perkins and Williams (2002) and Williams et al. (2004).

Another essential aspect in the simulation is the calculation of sub-lattice forces using multiple sub-time steps. Depending on the concentration of solids, either constant or adaptive (variable) sub-time steps were used, viz a constant sub-time step for dilute and moderately dense suspensions up to 36% solids, and an adaptive time-stepping scheme for more dense cases ($\phi_v > 40\%$). In the latter scheme, if overlap between two particles or between a particle and either wall was observed, the calculation of LC and DLVO forces and integration of particle motion was repeated by doubling the number of sub-time steps until the point that no overlap occurred. If no overlap is found in the next fluid time step, n_{tp} is halved by the value used in the previous fluid time step. In this manner, the algorithm adapts the number of sub-time steps and resolves the sub-lattice scale interactions. The number of sub-time steps in the simulations with ϕ_v ranging from 6 to 36% was kept constant between 50 and 200. However, for suspensions containing 43 and 52% solids, the latter approach used about 512 sub-time steps.

Table 1
Variables and values used for implementing the Van der Waals and EDL forces in the simulation are given for the particles with physical radii of 10 and 150 μm dispersed in a symmetric electrolyte (e.g. NaOH) solution with pH = 11 and $I = 10^{-3}$ mol/L. The unit of length, time, and mass is expressed as lu, ts and mu, respectively. Variables like lu, R, A_H, κ^{-1}, etc. are divided into two rows where the value in the top row corresponds to 10 μm particle size, while the bottom row corresponds to 150 μm. The value of $k_B T$ in physical units specified in this Table is for 0 °C.

Variable	Description	Physical units	LB units
ν	Kinematic viscosity	10^{-6} m^2 s^{-1}	1/30 lu^2 ts^{-1}
ρ	Fluid density	1000 kg m^{-3}	1 mu lu^{-3}
lu	Lattice spacing	1.25×10^{-6} m 1.875×10^{-5} m	1 lu
R	Particle radius	10×10^{-6} m 150×10^{-6} m	8 lu
ts	Lattice time	5.2×10^{-8} s 1.17×10^{-5} s	1 ts
$\dot{\gamma}$	Shear rate	807 s^{-1} 3.6 s^{-1}	4.2×10^{-5} ts^{-1}
A_H	Hamaker constant	9.54×10^{-20} J	4.44×10^{-9} mu lu^2 ts^{-2} 2.96×10^{-10} mu lu^2 ts^{-2}
κ^{-1}	Debye length	9.61×10^{-9} m	1/130 lu 1/1950 lu
$k_B T$	Boltzmann constant × T	3.771×10^{-21} J	3.4×10^{-9} mu lu^2 ts^{-2} 2.23×10^{-10} mu lu^2 ts^{-2}
η_∞	Number density	6.022×10^{23} m^{-3}	1.17×10^6 lu^{-3} 3.97×10^9 lu^{-3}

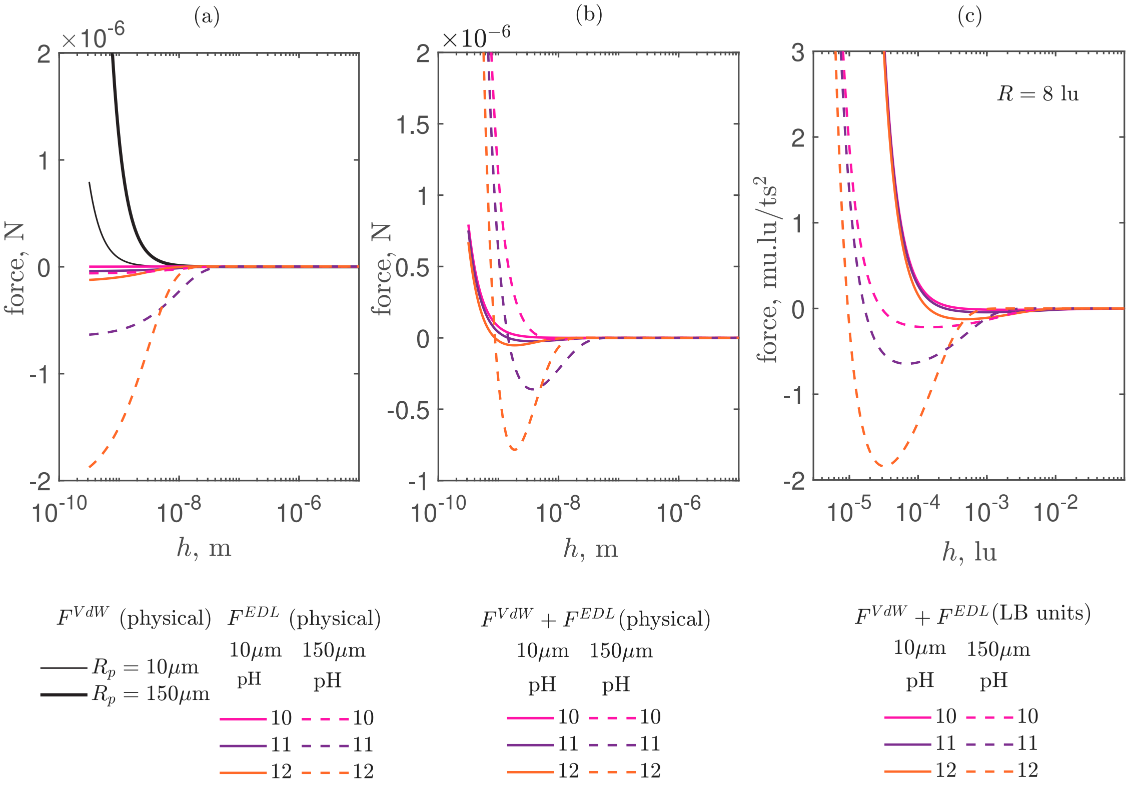

Fig. 1. Left panel: individual contributions of the physical Van der Waals and EDL forces are shown for particles with physical radii of 10 and 150 μm, respectively. The middle panel shows the overall (‘$F^{VdW} + F^{EDL}$’) contribution of the physical Van der Waals and EDL force. Right panel shows the total interaction force in LB units for $R = 8$ lu, and other corresponding parameters as given in Table 1. The pH = 10, 11, and 12 is the same in all panels.

Although these sub-lattice forces could have been computed implicitly during sub-cycling, as demonstrated by Nguyen and Ladd (2002), an explicit scheme was sufficiently accurate for our purposes.

2.4. Simulations

The simulation cases discussed in this paper are as follows

- analysing the collision dynamics of two spheres under the influence of both LC and DLVO forces (Section 3).
- simulating suspensions to elucidate the rheology, clustering dynamics, and particle structuring (Section 4).

In all these cases, we used equally sized particles with an input radius of 8 lu. The domains were periodic in streamwise x and spanwise y directions. In the discussion of the simulations in Section 3.1 and Appendix, the walls (top and bottom) were stationary, while the walls translate in opposite directions in the simulations discussed in Sections 3.2 and 4. In these simulations, an effective (or *hydrodynamic*) radius was used to compute the interparticle and particle–wall collisions. The calculation of an effective radius has been previously reported by several other authors (Rohde et al., 2002; Ten Cate et al., 2002; Feng and Michaelides, 2009; Krüger et al., 2011; Srinivasan et al., 2020a). All of these implementations of moving surface boundary conditions encountered an increase of R_{hyd} between 0.2 and 1 lu. Also, in our simulation, we noticed that the hydrodynamic radius increased by around 8% ($R_{hyd} = 8.65$ lu) relative to the input radius.

In all simulations discussed in this paper, particles were simulated with densities twice that of the fluid density, $\rho_f = 1$ (in lattice units). The density of the solid is $\rho_s = \rho_p + \rho_f$, where, ρ_p is the additional density of the particle (Derksen and Sundaresan, 2007). All simulations used $\rho_p = 1$, therefore the density ratio is $\sigma = \rho_s/\rho_f = 2$ (Srinivasan et al., 2021).

3. Collision dynamics of two spheres with DLVO forces

3.1. Determination of equilibrium gap

This section focuses on the collision dynamics of two equally-sized spheres under the influence of DLVO forces, demonstrating how the gap size evolves over time. For this purpose, we consider two simulations in which the initial gap (along the x direction), h_o, between the spheres is 0.001 lu in the first case and 0.007 lu in the second case. In both simulations, the y and z positions of the colliding particles were equal, and therefore, the particle motion is not influenced by tangential forces. Liquid kinematic viscosity was 1/6 lu^2/ts and rotational motions are inhibited in both simulations. Due to the inclusion of normal LC, oscillations do not occur and the position of the particle approaches the equilibrium position steadily.

The cutoff distance at which the EDL and Van der Waals forces were turned on was the same as used for the normal LC because these forces were found to be relevant for much smaller gap sizes of O(0.01). As shown in Appendix A.2.1, the normal LC is switched on at the cutoff distance of O(0.1), and therefore, it is reasonable to turn on the DLVO forces over the same order of magnitude as normal LC. The inverse Debye length used in this simulation was 1950 lu^{-1}. Since the particle resolution was set at 8 lu we rescale the Debye length in LB units to account for particles with physical radii of 10 and 150 μm respectively (see Table 1). For convenience, we normalise these inverse Debye lengths by the hydrodynamic radius to form the non-dimensional Debye length, κR_{hyd}. In all the simulations that follow, for a fixed pH of 11, we vary κR_{hyd} in order to study its effect on (a) the collision dynamics of two spheres and (b) the rheology and structure of suspensions.

Fig. 2 presents the evolution of the dimensionless gap size as a result of the collision between two spheres as a function of simulation time t normalised by the viscous time scale based on R_{hyd}. For the parameters specified in Table 1 for 150 μm particles, h_{eq} is calculated to be 0.705×10^{-3} lu (solid line in Fig. 2). As expected, the gap size computed from the simulation increases to reach the equilibrium value when h_o is 0.001 lu, while with a larger initial gap, the gap size decreases to attain equilibrium.

3.2. Effect of shear

While the particles were moved by the balance of forces in the previous case, now we study the effect of shear on collisions between two spheres. The purpose of this simulation is to compare the trajectories of particles colliding under simple shear flow conditions in simulations with and without DLVO forces activated. The wall velocity U_w was set such that the particle Reynolds number, $Re_p = \dot{\gamma} R_{hyd}^2/\nu$, is 0.1 and shear rate, $\dot{\gamma} = 2U_w/H$, is 4.5×10^{-5} ts^{-1}. The resolution of the computational grid and particle radius was twice that of our previous study (Srinivasan et al., 2020a) with a confinement ratio, $\delta = 2R_{hyd}/H \approx 0.11$. Translation and rotation of two spheres with an initial centre-centre distance of $10R$ and $2.5R$ in the directions of x and z were simulated for 500,000 iterations. The kinematic viscosity was 1/30 lu^2/ts and $\kappa R_{hyd} = 1124$ and $16\,867$.

A sample 3-D visualisation of the liquid flow field and two spheres (after collision) is shown in the left panel of Fig. 3. Results shown at the right panel of Fig. 3 are the trajectories of either particle under the influence of successive additions of only EDL (blue lines), EDL and Van der Waals (red lines) and the combination of EDL, Van der Waals, and LCs (green lines), respectively. The second particle has the same trajectory as presented in Fig. 3 though in the opposite direction, and is not shown.

When the shear flow starts, the flow develops from either wall, and open trajectories are more commonly encountered as the spheres approach (Van de Ven, 1982), i.e. two particles approach and pass each other from opposite directions. We distinguish the dynamics of particle collisions into two stages. The first is the approach stage, where two particles come closer from the opposite directions as $(x - x_m)/R < 0$, and the second is the separation stage, $(x - x_m)/R > 0$. We can see that the dynamics of the post-collision trajectories (i.e. the separation stage) in the present work are very different from the previous case of just hydrodynamic (LB, excluding LC) forces (dotted magenta line). As κR_{hyd} increases, we realise that the strength of the EDL force reduces (see Eq. (2)). As a result, the particle is repelled to a shorter distance (as seen from the dash–dot green line at the bottom panel of Fig. 3). When comparing the separate effects of EDL (solid blue lines) and EDL plus Van der Waals (dashed red lines) force, it is evident that the contribution of the Van der Waals force does not significantly affect the post-collision particle trajectory. As far as our simulations are concerned, the attractive forces are always overpowered by the contribution of EDL forces, indicating that the inclusion of surface charges has a substantial effect on particle trajectories at these conditions.

4. Suspension rheology

Suspension simulations for several solids volume fractions between 6 and 52% were conducted with the effects of including sub-lattice scale forces under a constant shear rate. In these simulations, the particles are initially arranged in a cubic lattice with small random displacements. The size of the simulation box is $L \times W \times H$ (where $L = 208$ lu and $W = H = 104$ lu are the lengths, width, and height of the simulation box, respectively). Other simulation parameters are the hydrodynamic radius $R_{hyd} = 8.65$ lu, the confinement ratio $\delta = 0.166$, and the liquid kinematic viscosity $\nu = 1/30$ lu^2/ts. The wall speed is below the velocity of sound and did not surpass 0.01 lu/ts thus simulating an incompressible flow with particle Reynolds number, $Re_p = 0.1$. All simulations ran for at least one million time steps with $\dot{\gamma} t \approx 42.3$ on the national HPC system ICHEC (Irish Centre for High-End Computing) with several days for each simulation.

4.1. Relative apparent viscosity

The effect of including LC and DLVO forces on relative apparent viscosity is demonstrated in terms of time-evolution and as a function of solids volume fraction. In the remainder of this section (Sections 4.2.1 and 4.2.2) we will interpret our viscosity data in terms of particle clusters, and the formation of particle layers and structures. First of all, the relative apparent viscosity is computed from the top and bottom walls as (Srinivasan et al., 2020a)

$$\eta_r = \frac{\langle \tau_w^{LB} \rangle + \tau_w^{lub}}{\mu \dot{\gamma}} \tag{7}$$

where $\tau_w^{LB} = \mu \frac{U_w - U_{xw}}{\Delta y}$ is the local LB shear stress on the walls (μ is the dynamic fluid viscosity, U_{xw} is the x component of the liquid velocity adjacent to either wall, and $\Delta y = 0.5$ is the distance between the wall and the neighbouring fluid node). $\langle\ \rangle$ denotes the average of wall

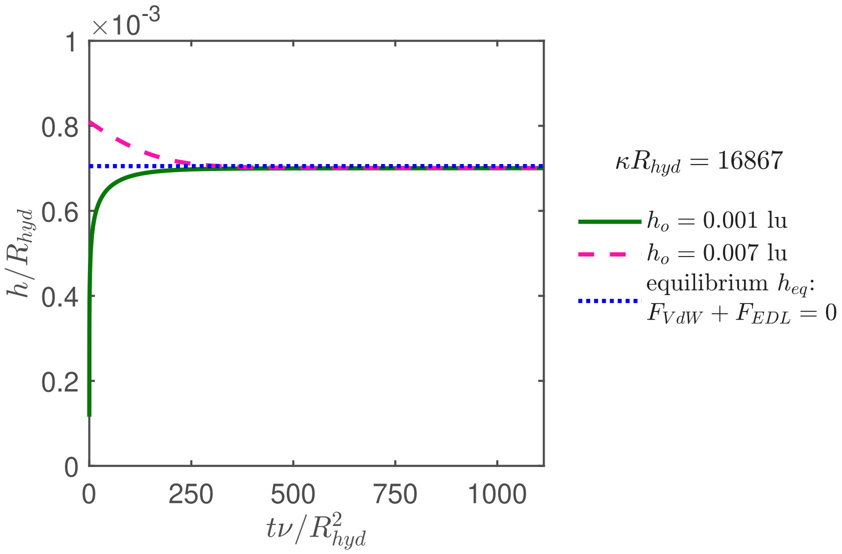

Fig. 2. Comparison of the evolution of dimensionless gaps as a function of $t\nu/R_{hyd}^2$ is shown for two simulations starting from different initial separation distances, $h_o = 0.001$ (solid green line) and 0.007 lu (dashed green line), respectively. The solid line indicates the equilibrium gap, h_{eq} where the sum of the forces (i.e. Van der Waals and EDL) on the particles become zero.

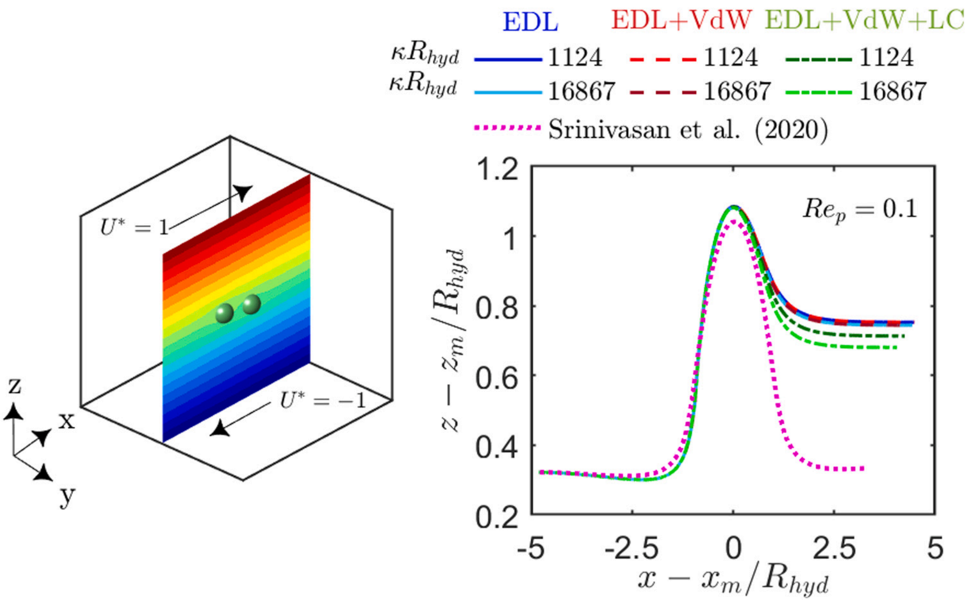

Fig. 3. Left panel: 3-D visualisation of two spheres after collision under simple shear flow with $\dot{\gamma}$ and $U^* = U_x/U_w$ (where U_x is the liquid velocity in the x direction) being the shear rate and dimensionless liquid velocity. Right panel shows the comparison of the influence of sub-lattice forces on the particle trajectory with the simulation of Srinivasan et al. (2020a) in an interstitial liquid with $Re_p = 0.1$. The parameters $x_m = L/2$ and $z_m = H/2$ indicate the simulation domain centres, and the arrow indicates the direction of the sphere's motion. The black dot below the arrow shows the starting position of the sphere. (For interpretation of the references to colour in this figure legend, the reader is referred to the web version of this article.)

shear stress being computed over the $x-y$ cross-section. The tangential lubrication stress on the walls is $\tau_w^{lub} = \frac{1}{LW}\sum(\mathbf{F}_p^{w,tt} + \mathbf{F}_p^{w,tr})$ (see Appendix for the expressions of $\mathbf{F}_p^{w,tt}$ and $\mathbf{F}_p^{w,tr}$). The viscosity values from either wall are then combined to obtain an average relative apparent viscosity (which we denote as $\bar{\eta}_r$). This average (of top and bottom wall) viscosity fluctuates over time (see Section 4.1.1), and therefore the time-averaged viscosity over the period of steady fluctuations (which we denote as $\bar{\bar{\eta}}_r$) is reported in Section 4.1.2. It is important to note that both the Van der Waals and EDL forces act normal to the wall and therefore do not contribute to the shear stress directly. These forces affect the suspension structure (as discussed in Section 4.2.2), which indirectly affects the shear stress.

4.1.1. Time-evolution of $\bar{\eta}_r$

First, the evolution of average relative apparent viscosity, $\bar{\eta}_r$, as a function of non-dimensional time (starting from rest) is presented in Fig. 4 for a suspension with 30% solids obtained by including Van der Waals, EDL, and lubrication forces in varying combinations. For all cases, it is evident that as time evolves, the average viscosity first decreases to a minimum (approximately 2) and then increases to attain a stable value after about 15–20 strain times. The time-averaged ($21 \leq \dot{\gamma}t \leq 42$) viscosity obtained from the simulation in the absence of EDL forces ($\kappa R_{hyd} = \infty$: solid red line) is approximately 3.4. By adding the EDL forces with LC forces, the steady viscosity of the suspension decreases by approximately 18 and 26% for varying magnitudes of $\kappa R_{hyd} = 16\,867$ (solid green line) and 1124 (solid blue line), respectively. By adding Van der Waals forces (as indicated by the

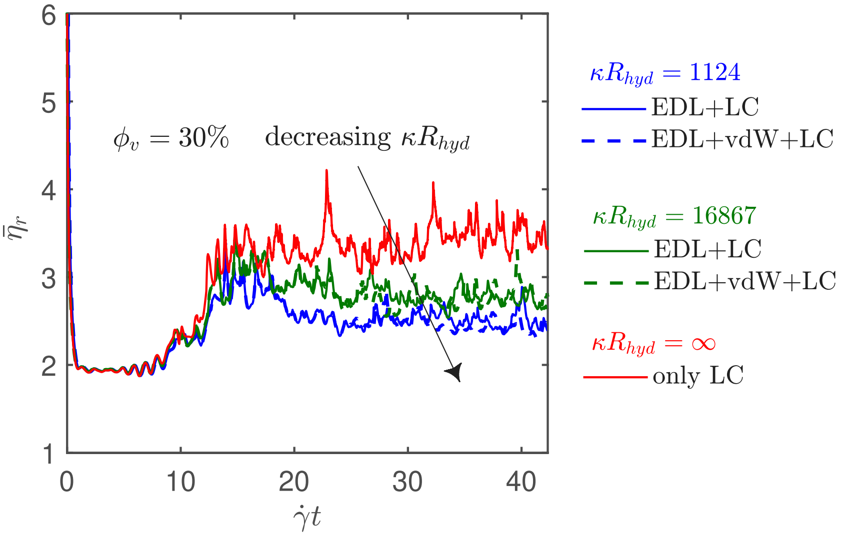

Fig. 4. The effect of κR_{hyd} on the time-evolution of the relative apparent viscosity of a suspension with 30% solids is shown for several sub-lattice scale forces. The particle Reynolds number Re_p was 0.1 in all simulations. The dimensionless Debye lengths κR_{hyd} were 1124, 16 867, and ∞ (which implies the absence of EDL force), respectively. (For interpretation of the references to colour in this figure legend, the reader is referred to the web version of this article.)

dashed green and blue lines), we can see that the viscosity variations are different though without any noticeable change in the average value. Even for 52% solids, it was found that the inclusion of Van der Waals forces had no impact on the average viscosity of the suspension. We therefore conclude that the influence of attractive Van der Waals forces does not affect the relative viscosity of the suspension, at least for our simulation conditions. In all results presented from now onward, we will thus ignore the contribution of the Van der Waals force and consider only the sub-lattice scale corrections from EDL and lubrication forces and torques.

Now we turn our attention to discuss the time-evolution of viscosity of a suspension with 52% solids with only EDL and LC. In these simulations, the suspensions are sheared for longer periods up to $\dot{\gamma}t \approx 105$ compared to the previous case. From Eq. (7), we know that the relative apparent viscosity of the suspension is expressed as the summation of the resolved LBM and unresolved lubrication viscosity. Therefore, in Fig. 5, we compare how these individual fluid (LBM) and particle (lubrication) viscosities contribute to the total viscosity of the suspension for two separate values of κR_{hyd}. In either case, we can see that the viscosity fluctuates initially at some rate. For $\kappa R_{hyd} = 16\,867$, the total average apparent viscosity (green line) wavers until $\dot{\gamma}t \approx 27$. Once the initial cubic structure is set into motion and collapses, the stresses build and the momentum transport rate increases that – in turn – rapidly increases the relative apparent viscosity. After the first increase, we observe that the viscosity then gradually ramps down from approximately 10 to 6 between times $40 \leq \dot{\gamma}t \leq 70$, and then stabilises till the end of shearing. On the contrary, for the case shown in the left of Fig. 5 (i.e. $\kappa R_{hyd} = 1124$), we can see that the viscosity first oscillates continuously until $\dot{\gamma}t \approx 60$ before it increases to approximately 7.5 and decreases to attain a steady viscosity of approximately 5. These long steady initial oscillations observed for a lower magnitude of κR_{hyd} (or higher Debye lengths) suggest that the suspension takes longer periods to break the initial particle assembly and re-structure into a new configuration. Comparing the results between rather dilute (see Fig. 4) and dense (see Fig. 5) suspensions, the response time of suspensions after imposing a shear flow or shear stress, increases with increasing solid fractions.

4.1.2. Effects of particle concentration

Having presented the time-evolution of viscosity for two solids loadings (30 and 52%), we now discuss the time-averaged relative apparent viscosity which we denote as $\bar{\bar{\eta}}_r$ for a wider range of ϕ_v between 6 and 52%. For all concentrations (including $\kappa R_{hyd} = \infty$), suspensions were sheared up to $\dot{\gamma}t \approx 42$ and the time-averaged viscosities were obtained between $21 \leq \dot{\gamma}t \leq 42$. However, in the case of $\phi_v = 52\%$ with EDL forces, the simulations ran until $\dot{\gamma}t \approx 105$ (as stated earlier) and the viscosity average was between $70 \leq \dot{\gamma}t \leq 105$ and $90 \leq \dot{\gamma}t \leq 105$ for $\kappa R_{hyd} = 16\,867$ and 1124, respectively.

Fig. 6 presents the dependence of $\bar{\bar{\eta}}_r$ on ϕ_v. The simulation results of the present study (filled left, up, and down-pointing triangles in red, green, and navy blue) are compared with the correlation of Krieger and Dougherty (1959), experiments of Dbouk et al. (2013), Stokesian dynamics simulations of Sierou and Brady (2002), LB simulations with repulsive spring force by Thorimbert et al. (2018), Srinivasan et al. (2020a), and finally LB simulations with normal and tangential LC in which the hydrodynamic radius of the particle was 4.2 lu (Srinivasan et al., 2021).

First, we compare $\bar{\bar{\eta}}_r$ with the results from only LC. Our earlier simulation results (Srinivasan et al., 2021), represented by right-pointing magenta triangles and obtained with an input radius of $R = 4$ lu ($R_{hyd} = 4.2$ lu) agree pretty well (for dilute concentration $\phi_v = 5\%$) with our current results represented by left-pointing red triangles and obtained with $R = 8$ lu ($R_{hyd} = 8.65$ lu). The solids volume fractions for the two cases are different because the ratio R_{hyd}/R differs. For $R_{hyd} = 8.65$ lu, the solids volume fraction is larger and therefore these data points appear to the right of those for $R_{hyd} = 4.2$ lu (see error bars for $\phi_v = 52\%$). These observations have led us to conclude that, with the same confinement ratio, the initial 4 lu radius used by us earlier provides sufficiently accurate results.

Now we compare the effects of subsequently adding the EDL forces to LCs and their consequences on $\bar{\bar{\eta}}_r$ as a function of ϕ_v. Form the up- and down-pointing triangles in green and navy blue in Fig. 6, it is evident that the addition of this extra force decreases the viscosity by a noticeable amount when $\phi_v \geq 30\%$. The viscosity reduces further when the magnitude of κR_{hyd} decreases. At 52% solids, the viscosity plateaus (as evident from the dotted lines that connect the triangles) to attain (almost) the same value as in 43% solids because at such high concentrations the room for the particles (that is, the mean centre-centre distance) to move freely decreases and the repulsive forces lock the configuration of the particle structure. The plateauing of relative suspension viscosity seen in Fig. 6 is explained in terms of particle structures in Fig. 8. For ϕ_v up to 36%, the viscosities presented in navy blue and green are in close agreement with the spring simulations of our previous work (Srinivasan et al., 2020a). We speculate that in

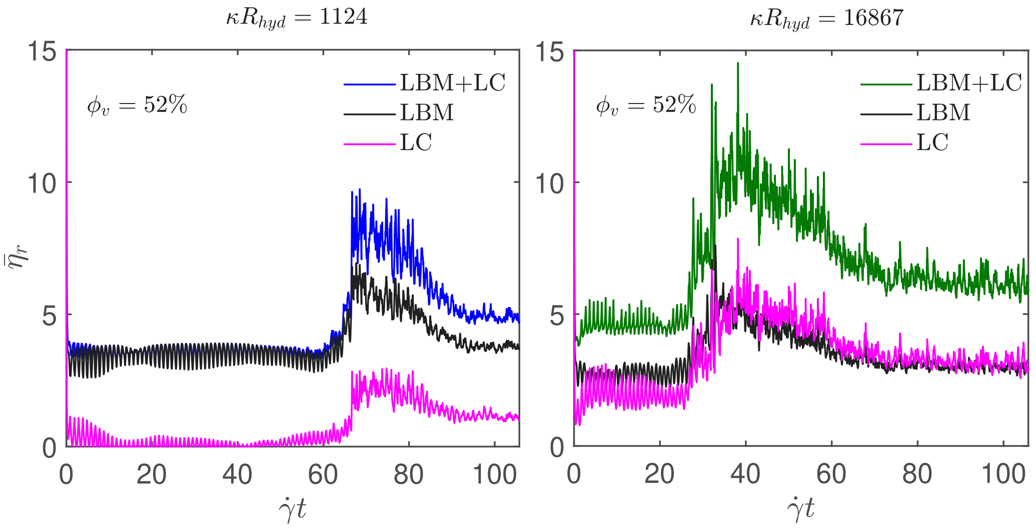

Fig. 5. Time-evolution of the average (of top and bottom wall) relative apparent viscosity of a suspension at 52% solids obtained by the contribution of only LBM (solid black line), only LC (solid magenta line), and the summation of both LBM and LC (solid green and blue lines) is shown for two different values of $\kappa R_{hyd} = 16\,867$ (top panel) and 1124 (bottom panel). In both cases, the particle Reynolds number, $Re_p = 0.1$. (For interpretation of the references to colour in this figure legend, the reader is referred to the web version of this article.)

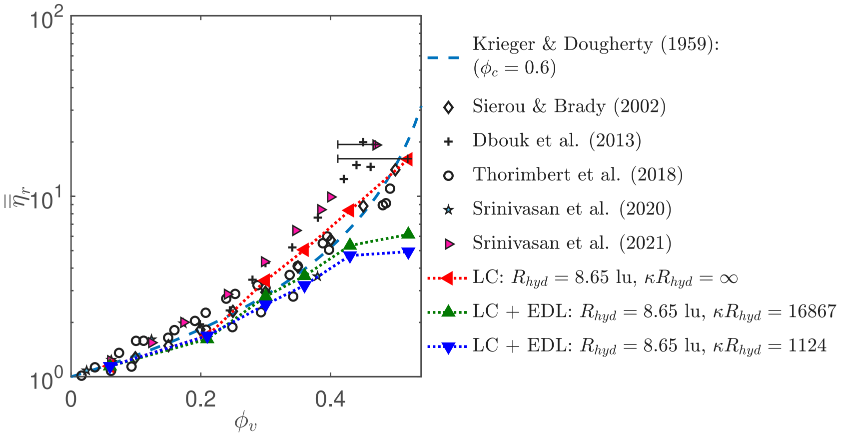

Fig. 6. Time-averaged relative apparent viscosities, $\bar{\bar{\eta}}_r$ as a function of solids volume concentration, ϕ_v between 2 and 52%. The particle Reynolds number, $Re_p = 0.1$. The dimensionless Debye length, $\kappa R_{hyd} = \infty$ (filled orange and red triangles) indicates the simulation of uncharged particles with R_{hyd} of 4.2 (Srinivasan et al., 2021) and 8.65 lu (current simulations), respectively. For the simulations with charged particles, the hydrodynamic radius was 8.65 lu and $\kappa R_{hyd} = 16\,867$ (filled green triangles pointing upwards) and 1124 (filled navy blue triangles pointing downwards), respectively. These simulation viscosities are compared with Krieger and Dougherty (1959) (dashed line), Sierou and Brady (2002) (diamonds), Dbouk et al. (2013) (pluses), Thorimbert et al. (2018) (circles), Srinivasan et al. (2020a) (filled pentagons). The errorbars (magenta lines) indicate the average viscosity computed based on the input radius of two resolutions, $R = 4$ and 8 lu. (For interpretation of the references to colour in this figure legend, the reader is referred to the web version of this article.)

both cases, the presence of non-hydrodynamic forces keeps particles away from the surface, which decreases the shear stress and therefore the relative viscosity. These variations in viscosity are related with the spatial distribution of particle structures — details are given in the upcoming section.

While two different values of $\kappa R_{hyd} = 1124$ and $16\,867$ were used in all simulations so far, a sample simulation of suspensions at $\phi_v = 43\%$ with $\kappa R_{hyd} = 113$ was performed to test the degree to which the effect of non-dimensional Debye length plays a role in determining the relative apparent viscosity. We found that time-averaged viscosity was in line with the simulation of $\kappa R_{hyd} = 1124$ with an average deviation of less than 0.5%. We remark here that the viscosity remains unchanged for κR_{hyd} less than some critical value, which in our case is 1124.

4.2. Structure

Variations in the relative apparent viscosity found for different values of κR_{hyd} are further investigated by analysing the 3-D spatial distribution in terms of (a) cluster dynamics and (b) particle layering versus 3-D particle structures

4.2.1. Cluster dynamics

For the first analysis, the particles' structural distribution is qualitatively interpreted in the following ways: (a) analysing the average cluster size for several choice of cluster cutoff h_c normalised using R_{hyd} and (b) computing the dynamic evolution of particle clusters. For these analyses, the simulation data over the last 10 strain times was used. While there are many ways to characterise cluster distributions, such as by means of pair distribution function (Sierou and Brady, 2002; Srinivasan et al., 2021) or a icosahedral order parameter Q_6 (Kumaran, 2009), the present method qualitatively demonstrates the distribution of particle structures in 3-D space. Although the development of structures from transient to steady state may depend on the sub-lattice forces, the emphasis of this paper is on steady particle structures.

A cluster is defined as a group of particles where the distance between adjacent particle surfaces is smaller than h_c. For several values

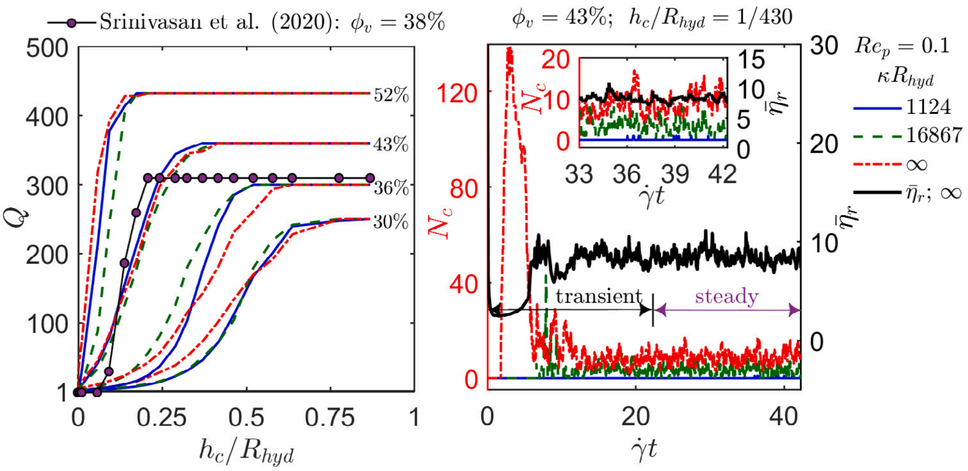

Fig. 7. Left panel: dependence of average cluster size during the last 10 simulation strain periods for $\phi_v = 30$, 36, 43, and 52% and $\kappa R_{hyd} = 1124$, 16 867, and ∞ is shown as a function of cluster threshold, h_c/R_{hyd} for $Re_p = 0.1$. The filled symbols demonstrate the cluster size distribution obtained by Srinivasan et al. (2020a). Right panel: time-evolution of the number of clusters (left axis) for $h_c/R_{hyd} = 1/430$ and $\bar{\eta}_r$ (right axis) are shown for 43% solids. Inset displays the steady evolution of both N_c and $\bar{\eta}_r$ over the last 10 strain times ($33 \leq \dot{\gamma}t \leq 42$).

of h_c, we compute the average cluster size as $Q = N_p N_s / N_c^t$, where N_c^t is the total number of clusters (including all individual particles) counted over N_s equally-spaced samples of the simulation state. The value of Q is always between 1 and N_p; this means that when $Q = 1$ there are no clusters, while $Q = N_p$ indicates that all particles are counted as one cluster. In between 1 and N_p, the cluster size depends on the choice of h_c. Since the selection of h_c is arbitrary, we consider the effect of h_c on the size and number of clusters. The dependence of the number of clusters on h_c provides information on how the particles are distributed in space. While computing the average cluster size, we use the data over the last 10 strain times of the simulation state.

Fig. 7 presents the dependence of Q as a function of h_c/R_{hyd} for four different solids loading (i.e. 30, 36, 43, and 52%) and one particle Reynolds number, $Re_p = 0.1$. For each solids concentration, Q is compared for three values of κR_{hyd}, i.e. 1124 (blue lines), 16 867 (dashed green lines), and ∞ (dash–dot red lines), respectively. As the concentration of solids increases from 30 to 52%, we can see that the average cluster size also increases with increasing cluster threshold (see the narrow distribution of gap sizes in left panel of Fig. 7). Once h_c exceeds a critical gap between the surface of the sphere, Q saturates to match the number of particles as h_c is large enough that all particles are counted as being in one cluster. This critical gap is determined by the length of the Debye layer as it holds the particles apart over the Debye length. In the discussion that follows, we will show how clusters evolve as a function of time when the cluster threshold is chosen to be the same order of magnitude as the Debye length.

Along with these solid, dashed, and dash–dot lines, the dependency of Q as a function of h_c/R_{hyd} for a suspension at 38% solids (Srinivasan et al., 2020a) is also shown in filled symbols. In our previous simulation, a spring-like, non-hydrodynamic repulsive force was used between adjacent particles to model interparticle interactions, where the spring forces were turned on when the gap between the particles is less than 1 lu. Comparing the trends between our current simulation (EDL at 36% solids) and our previous analysis (spring force at 38% solids), in either case up to $h_c/R_{hyd} \approx 0.05$, we can see that Q is approximately 1. This means that the influence of non-hydrodynamic forces prevents particles from forming clusters over a certain cutoff distance (determined by the spring threshold in the previous case and Debye length in the present case) and alters the morphology of the suspension.

Presented in the right panel of Fig. 7 is the temporal evolution of N_c (left axis) and $\bar{\eta}_r$ (right axis — for $\kappa R_{hyd} = \infty$) for $\phi_v = 43\%$ and $Re_p = 0.1$. First of all, N_c is calculated by identifying pairs of particles that touch each other's surface over the same N_s samples as before. With respect to the dynamics of cluster evolution, two regions may be discerned, viz. the initial development from rest ($0 \leq \dot{\gamma}t < 21$) and the steady-state region ($21 \leq \dot{\gamma}t \leq 42$) - as indicated by the black and purple arrows. In this paper, we focus on the steady-state clusters, and the analysis of the initial development of clusters is left for the future. Between the two Debye lengths discussed in this paper (see Table 1), a cluster threshold of 1/430 is chosen to demonstrate its effect on the number of clusters. Comparing the time-evolution of $\bar{\eta}_r$ and N_c, it is evident that the time scales of the both evolution are the same. After around 10 strain times, both $\bar{\eta}_r$ and N_c start to hit a stable value. From the inset that displays the steady evolution of $\bar{\eta}_r$ and N_c over the last 10 $\dot{\gamma}t$ of the simulation state, we can hardly see any clusters for the case with $\kappa R_{hyd} = 1124$. Since the selected cluster threshold ($h_c/R_{hyd} = 1/430$) is within the same order of magnitude as the Debye length ($\kappa^{-1} = 1/130$ lu), the particles are held apart from each other. However, as the Debye length decreases, the EDL forces weaken and the contribution of LC governs the cluster formation. As a result, we can see approximately 10 clusters when $\kappa R_{hyd} = \infty$. As clusters accelerate momentum transfer, the higher their number the higher the relative apparent viscosity.

4.2.2. Particle structuring and ordering transitions

Now we go on to investigate the differences in apparent viscosity by studying the spatial distribution and structuring of particles in dense shear flow. Yeo and Maxey (2010) distinguished between the spatial variation of particles into three regimes. The first is the particle layering regime that happens predominantly near the walls, and the second is the core region where the suspensions are homogeneously mixed. In between the core and either wall is the buffer region that has the features of either regime.

The particle Reynolds number $Re_p = 0.1$ was kept constant, and we compare in Fig. 8, the cases for varying $\kappa R_{hyd} = 1124$ (top), 16 867 (middle), and ∞ (bottom), respectively. The 3-D sample visualisation ($x-z$ view) of the suspended particles at the end of the simulation state is shown in the left panel of Fig. 8 for $\phi_v = 43$ and 52%. In all snapshots, the spheres are drawn at half ($R = 4$ lu) the original size (i.e. 8 lu) to display the distribution of particles clearly. In either case, near the walls, we can see that the particle layers are predominant. For relatively dilute suspensions, $\phi_v = 43\%$, as we pass away from either wall, the layers disappear and structures formed are homogeneously distributed in the core of the flow (i.e. the centre of the simulation domain). In between wall and core, the particles tend to form both layers and homogeneous structures. For dense suspensions, (i.e. $\phi_v = 52\%$), one can see layers of particles (in all zones: near the walls, buffer zone and the core)

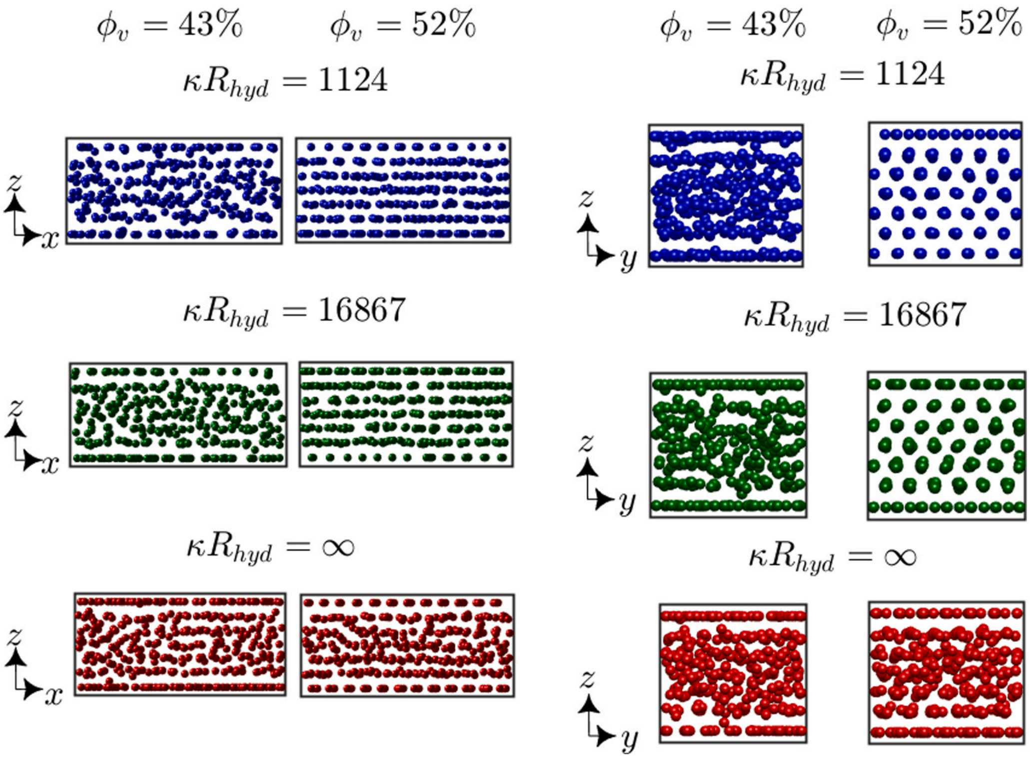

Fig. 8. Left panel: $x - z$ visualisations of particles are shown for $\phi_v = 43$ and 52%. Right panel: $y - z$ visualisations of suspended particles with 43 and 52% solids are compared. In both panels, from top to bottom, the magnitude of κR_{hyd} increases from 1124 to ∞. The radius of each sphere is drawn half of its original size and the particle Reynolds number $Re_p = 0.1$. (For interpretation of the references to colour in this figure legend, the reader is referred to the web version of this article.)

in the presence of EDL forces; interestingly, the suspensions look well-mixed in the core region when EDL forces are absent (i.e. $\kappa R_{hyd} = \infty$). Furthermore, since the space for particles to move freely is restricted at 52% solids, the EDL repulsive potential around the spheres pushes the particles apart, causing sliding layers to form (as shown in the second column of Fig. 8 for $\kappa R_{hyd} = 1124$ and 16 867, respectively). As a result of this repulsive potential, microstructures emerge to minimise energy dissipation, which can be interpreted as a way to decrease apparent viscosity and facilitate transport in pipelines.

By visualising the particles from the $y - z$ perspective as shown in the right panel of Fig. 8, the difference in the structuring of suspended particles can be seen when the loading of solids increases from 43 to 52%. In all these snapshots, the distribution of particles shown is at the end of the simulation. For all magnitudes of κR_{hyd}, at 43% solids, particle layering is clearly visible near either wall, while in the core region, the particles form chain-like structures. As the solids volume fraction increases from 43 to 52%, for $\kappa R_{hyd} = 1124$ and 16 867 (top and middle row in the right most panel of Fig. 8), a clear transition in the structuring of particles from homogeneous chains to hexagons is observed. It is interesting that this type of structural transformation is only observed when EDL forces are present. For $\kappa R_{hyd} = \infty$, although layers are seen near the walls, at the core region the particles are smeared and the structures are not as distinctly visible as observed for the other two values of κR_{hyd}. Although it is intuitive that increasing the solids volume fraction increases the apparent viscosity, the contribution of EDL repulsive forces is significant enough that the particles are held apart, lowering the local shear stress and thus the relative viscosity, explaining why the plateauing behaviour occurs. From Fig. 5, we know that in the presence of the EDL force the simulation took around 105 strain times to achieve a steady viscosity value. We remark here that, in the absence of the EDL force, the suspension took approximately $\dot{\gamma}t = 43$ to achieve an equilibrium structure with no qualitative change in the particle ordering for $\phi_v = 43$ and 52%. In either case, the structures in the core region are homogeneously mixed, which promotes momentum transfer and increases the viscosity.

We quantitatively evaluate the ordering transitions for the last 10 strain times of the simulation by first computing the time-averaged area fractions, $\overline{\overline{\phi}}_a$ at 43% solids, and then demonstrating the spatial variation of particles at 52%. Presented in the left panel of Fig. 9 are the comparisons of $\overline{\overline{\phi}}_a$ as a function of normalised channel height z/R_{hyd} for several values of κR_{hyd} at 43% solids. In all cases, we can see that the peaks are higher in the vicinity of the walls, while they are noticeably higher when EDL forces (navy blue and green lines) are included. These peaks indicate the evidence of particle-layering near the walls. However, as κR_{hyd} increases, the values of the peak near the walls decrease. After the first peak, the subsequent peaks drop dramatically from approximately 0.6 to 0.4. In the core region, we can see that all simulations have a similar trend in the distribution of $\overline{\overline{\phi}}_a$ with an average value of ≈0.37.

The results of the present simulation are validated by comparing the time-average area fractions of our work (LBM with LC and EDL forces) with Force Coupling Method (FCM) simulations with LC and contact forces of Yeo and Maxey (2010) at $\phi_v = 40\%$ (pluses in the left panel of Fig. 9). While the simulations of Yeo and Maxey (2010) are under Stokes flow conditions ($Re_p \ll 1$) with $\delta = 0.1$, in our simulations, the particles are rather larger in size with finite inertia ($Re_p = 0.1$), and the confinement ratio is 0.166. The peak and base values are comparable with Yeo and Maxey (2010) up to the buffer region (i.e. $z/R_{hyd} \approx 4$). At the core, the structures are different, indicating that the impact of confinement affects the spatial distribution of particles.

In the case of a dense suspension (i.e. $\phi_v = 52\%$), as seen from the navy blue and green lines in the right panel of Fig. 9, the number of peaks corresponds to the number of layers observed in the rightmost top and middle rows of Fig. 8. Since the particles appear to be smeared in the core region for simulations with $\kappa R_{hyd} = \infty$, we can see that the distribution of particles in space follows a similar pattern to that seen in $\phi_v = 43\%$. This advises that the presence of EDL forces significantly alters the structuring and spatial distribution of particle assemblies.

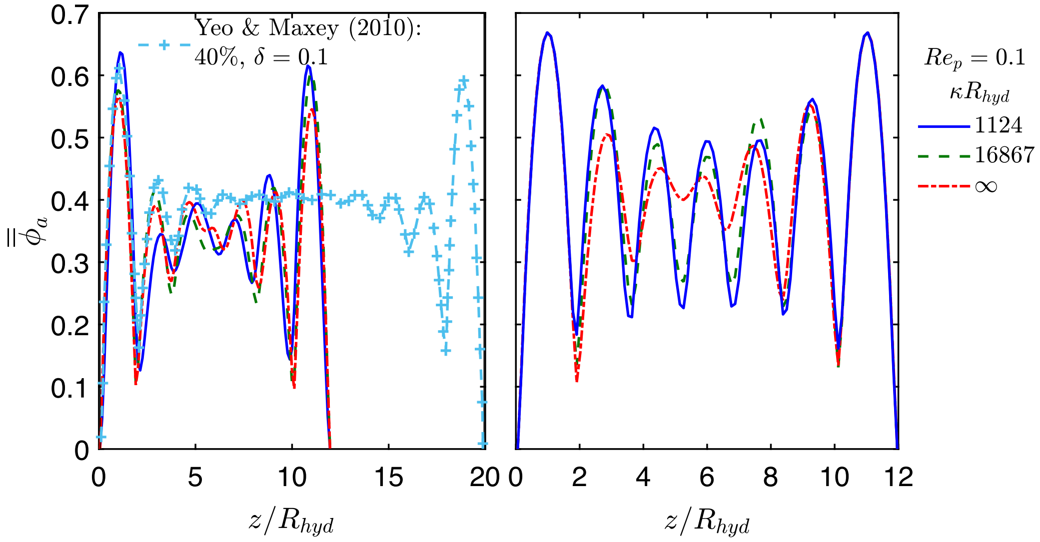

Fig. 9. The comparison of spatial variation of particles for several values of κR_{hyd} as a function of normalised channel height, z/R_{hyd} is shown for 43 (left panel) and 52% (right panel) solids. Shown in symbols (pluses) are the results of $\bar{\bar{\phi}}_a$ obtained by Yeo and Maxey (2010) for Stokes flow FCM simulations with LC and contact force model with $\delta = 0.1$ and $\phi_v = 40\%$.

With LCs alone, the suspended particles are homogeneously mixed and facilitate a higher rate of momentum transfer which, in turn, increases the relative viscosity of the suspension. These differences in the spatial distribution of particles with varying values of non-dimensional Debye lengths can underpin the variations in suspension viscosity.

5. Conclusions

Motivated by the hydraulic transport of electrically charged particles, three-dimensional direct numerical simulations of suspensions in aqueous electrolytes were performed under simple shear flow using a custom immersed boundary-lattice Boltzmann method code. Suspensions with varying concentrations of solids, ϕ_v between 6 and 52%, and a single particle Reynolds number, $Re_p = 0.1$, were simulated. Besides the hydrodynamics resolved in the LB lattice, the unresolved sub-lattice scale collisions are modelled by including corrections due to both hydrodynamic and non-hydrodynamic forces. In terms of hydrodynamic corrections, normal and tangential lubrication forces and torques were used, while electric double layer (EDL) and Van der Waals forces were used to model the non-hydrodynamic interaction.

Simple shear flow simulations under the influence of both lubrication and non-contact forces were performed to examine the trajectories of two colliding spheres. For the particle Reynolds number $Re_p = 0.1$ the results showed that the effect of the attractive Van der Waals forces was often dominated by the contribution of the repulsive EDL force.

In the case of shear flow of suspensions, good agreement has been found between our viscosities and the literature for solids concentrations up to 52%. In addition, for ϕ_v up to 38%, the current viscosities with EDL forces are consistent with our previous findings (Srinivasan et al., 2020a), where, a non-hydrodynamic force was used to model sub-lattice scale interactions. With decreasing values of the Debye length, our simulations (for $\phi_v \geq 30\%$) show a reduction in the viscosity down to approximately 30% of the case with only lubrication correction. We quantified this reduction in viscosity by assessing the structural distribution of particle clusters. Dense suspensions with a lower magnitude of non-dimensional Debye length respond more slowly to the applied shear stress on the walls than dilute suspensions, as the former takes a long time to break the initial cubic assembly and delay the development of the wall shear stress and therefore the relative apparent viscosity.

Our results with respect to the cluster dynamics of charged suspensions show that the influence of EDL forces slows down the rate of cluster formation, which can be interpreted as a way to prevent a transport line from being clogged. Furthermore, the time scales of the evolution of both the relative apparent viscosity and the number of clusters were found to coincide for a dense suspension at $\phi_v = 43\%$. The variations in the spatial structure of these suspensions have also been studied. Upon increasing ϕ_v from 43 to 52%, chain-like homogeneous structures are transformed into hexagonal assemblies with the inclusion of EDL forces, while the suspension retains its chain structure in the absence of EDL force. As these homogeneous chains facilitate a higher mixing rate compared to structured hexagonal assemblies, the momentum transport increases that – in turn – increases the viscosity of the suspension. Overall, the differences observed in the structuring of the particles due to changes in the sub-lattice forces substantiate the variation in the suspension behaviour.

CRediT authorship contribution statement

Sudharsan Srinivasan: Conception and design of study, Acquisition of data, Analysis and/or interpretation of data, Writing – original draft, Writing – review & editing. **Harry E.A. Van den Akker:** Conception and design of study, Analysis and/or interpretation of data, Writing – review & editing. **Orest Shardt:** Conception and design of study, Analysis and/or interpretation of data, Writing – review & editing.

Declaration of competing interest

The authors declare that they have no known competing financial interests or personal relationships that could have appeared to influence the work reported in this paper.

Acknowledgements

This research was conducted with the financial support of the Synthesis and Solid State Pharmaceutical Centre (SSPC), funded by the Science Foundation Ireland (SFI) and co-funded by the European Regional Development Fund under Grant Number 14/SP/2750. O.S. acknowledges Azam Karimimamaghan for assistance with the implementation of the binning algorithm. We thank the Irish Centre for High-End Computing (ICHEC) for the provision of computational facilities and support. Approval of the version of the manuscript to be published: Sudharsan Srinivasan, Harry E. A. Van den Akker, Orest Shardt.

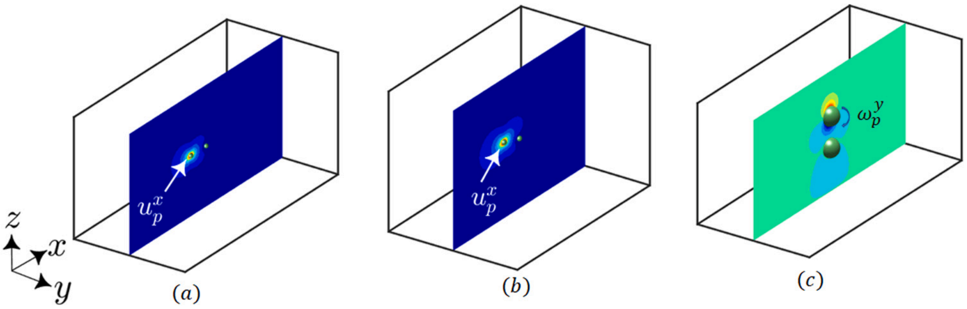

Fig. 10. Visualisations of translating and rotating rigid spheres are shown for the LC benchmarks. The particles have an equal radius of $R = 8$ lu. While the z position of the two spheres is equal in a, in b the translating particle is at a slightly higher z (one diameter distance) than the stationary particle. In a and b, the translating particle (shown with arrows) approaches the stationary particle with a constant speed of u_p^x, and in c, the upper particle rotates at a constant angular velocity ω_p^y. The background colours indicate the fluid velocity normalised by the particle speed.

Appendix

In this appendix, we first provide the governing equations used for implementing the LC forces and torques, followed by the benchmarks performed to determine the lubrication cutoffs.

A.1. LC modelling equations

First of all, the lubrication forces on particle p due to relative translation and rotation of spheres p and q can be written as (O'Neill and Majumdar, 1970; Simeonov and Calantoni, 2012)

$$\frac{\mathbf{F}_p^n}{6\pi\mu R_{hyd}^2} = \frac{\alpha^2}{(1+\alpha)^2}\left(\frac{1}{h}-\frac{1}{h_o^n}\right)\mathbf{U}_n \tag{A.1a}$$

$$\frac{\mathbf{F}_p^{tt}}{6\pi\mu R_{hyd}} = \left[\frac{4\alpha(2+\alpha+2\alpha^2)}{15(1+\alpha)^3}\ln\left(\frac{h}{h_o^t}\right)\right]\mathbf{U}_t \tag{A.1b}$$

$$\frac{\mathbf{F}_p^{tr}}{6\pi\mu R_{hyd}^2} = \left[\frac{2\alpha^2}{15(1+\alpha)^2}\ln\left(\frac{h}{h_o^r}\right)\right](\boldsymbol{\omega}^F \times \mathbf{n}_{pq}) \tag{A.1c}$$

where $\alpha = R_{hyd}^q/R_{hyd}^p$ is the ratio of radii, and $\mathbf{U}_n = (\mathbf{U}_{pq}\cdot\mathbf{n}_{pq})\mathbf{n}_{pq}$ (where $\mathbf{U}_{pq} = \mathbf{u}_q - \mathbf{u}_p$ is the relative translational velocity and $\mathbf{n}_{pq}$ is the unit vector) is the velocity along the unit normal. The velocity perpendicular to the unit normal is $\mathbf{U}_t = \mathbf{U}_{pq} - \mathbf{U}_n$. The relative rotational motion of the spheres is given by $\boldsymbol{\omega}^F = \boldsymbol{\omega}_{pq} + 4\alpha^{-1}\boldsymbol{\omega}_p + 4\alpha\boldsymbol{\omega}_q$ (where $\boldsymbol{\omega}_{pq} = \boldsymbol{\omega}_p + \boldsymbol{\omega}_q$). The superscripts n, tt, and tr denote normal, tangential translation, and tangential rotation, respectively. Following O'Neill and Majumdar (1970) and Simeonov and Calantoni (2012), the contribution from lubrication torques is written as

$$\frac{\mathbf{T}_p^{tt}}{8\pi\mu R_{hyd}^2} = \left[\frac{\alpha(4+\alpha)}{10(1+\alpha)^2}\ln\left(\frac{h}{h_o^t}\right)\right](\mathbf{n}_{pq}\times\mathbf{U}_{pq}) \tag{A.2a}$$

$$\frac{\mathbf{T}_p^{tr}}{8\pi\mu R_{hyd}^3} = \left[\frac{2\alpha}{5(1+\alpha)}\ln\left(\frac{h}{h_o^r}\right)\right]\boldsymbol{\omega}^T \tag{A.2b}$$

where $\boldsymbol{\omega}^T = \left(\boldsymbol{\omega}_p + \frac{\alpha\boldsymbol{\omega}_q}{4}\right) - \left[\left(\boldsymbol{\omega}_p + \frac{\alpha\boldsymbol{\omega}_q}{4}\right)\cdot\mathbf{n}_{pq}\right]\mathbf{n}_{pq}$.

During collisions, the particles not only interact with the neighbouring particles, but also come into contact with either the top and/or bottom walls. By having $\alpha \to \infty$ in Eqs. (A.1a) through (A.2b) and by replacing q with w, the lubrication forces and torques on particles throughout such contacts are derived as

$$\frac{\mathbf{F}_p^{w,n}}{6\pi\mu R_{hyd}^2} = \left(\frac{1}{h}-\frac{1}{h_o^n}\right)\mathbf{U}_n \tag{A.3a}$$

$$\frac{\mathbf{F}_p^{w,tt}}{6\pi\mu R_{hyd}} = \left(\frac{8}{15}\right)\ln\left(\frac{h}{h_o^t}\right)\mathbf{U}_t \tag{A.3b}$$

$$\frac{\mathbf{F}_p^{w,tr}}{6\pi\mu R_{hyd}^2} = \left(\frac{2}{15}\right)\ln\left(\frac{h}{h_o^r}\right)(\boldsymbol{\omega}^F\times\mathbf{n}_{pw}) \tag{A.3c}$$

and

$$\frac{\mathbf{T}_p^{w,tt}}{8\pi\mu R_{hyd}^2} = \left(\frac{1}{10}\right)\ln\left(\frac{h}{h_o^t}\right)(\mathbf{n}_{pw}\times\mathbf{U}_{pw}) \tag{A.4a}$$

$$\frac{\mathbf{T}_p^{w,tr}}{8\pi\mu R_{hyd}^3} = \left(\frac{2}{5}\right)\ln\left(\frac{h}{h_o^r}\right)\boldsymbol{\omega}^T \tag{A.4b}$$

In Eqs. (A.3a) through (A.4b), the definition of normal and tangential relative velocities remains the same as before, except that now q is replaced by w. All these forces and torques are summed up in order to obtain the overall LC contribution as

$$\mathbf{F}_p^{lub} = \mathbf{F}_p^n + \mathbf{F}_p^{tt} + \mathbf{F}_p^{tr} + \mathbf{F}_p^w \tag{A.5a}$$

$$\mathbf{T}_p^{lub} = \mathbf{T}_p^{tt} + \mathbf{T}_p^{tr} + \mathbf{T}_p^w. \tag{A.5b}$$

where $\mathbf{F}_p^w$ and $\mathbf{T}_p^w$ are summations of particle–wall LC (i.e. Eqs. (A.3a) through (A.3c) and Eqs. (A.4a) through (A.4b), respectively).

A.2. LC benchmarks

Now we move on to discuss the details of simulations carried out to determine the normal and tangential lubrication cutoffs required to appropriately evaluate the forces and torques on the particle over small interparticle gaps. We discuss the results of our simulations in the sequence shown in Fig. 10 by comparing with the literature. Two particles with equal radius have been used in these simulations. To this end, we calculate the forces and torques as a function of gap size and determine at what distances they become relevant.

The size of the simulation box in Fig. 10a and b were chosen to be large enough to prevent any periodicity effects. In order to achieve accurate forces and torques within the limit of large interparticle gaps, the confinement ratio in Fig. 10a and b were chosen to be ≈0.043 (where $H = 400$ lu is the height of the simulation box). For the simulation in Fig. 10c, a confinement ratio of 0.16 was adequate to achieve accurate results. However, in order to calculate the forces within the limit of small gaps, we use the correction expressions given in the previous section to account for the unresolved details of flow. Other parameters, such as density ratio (particle over fluid densities, $\sigma = \rho_p/\rho_f$) and ν, were 1 and 1/6 lu^2/ts, respectively.

A.2.1. Head-on collision: normal force

In this simulation, one particle is allowed to translate at a fixed speed in the positive x direction with translational particle Reynolds number $Re_p^t = u_p^x R_{hyd}/\nu = 0.025$ until surfaces touch. The second particle is stationary in the centre of the domain. The y and z components of the translating particle's velocity are set to zero. The spheres are separated by a centre-centre distance of $50R$ in the x direction with equal y and z positions.

Fig. 11 provides a comparison of the hydrodynamic (normal) force of both stationary (open circles) and moving (filled circles) particles obtained by LB simulation without LC and the analytical expression, viz.

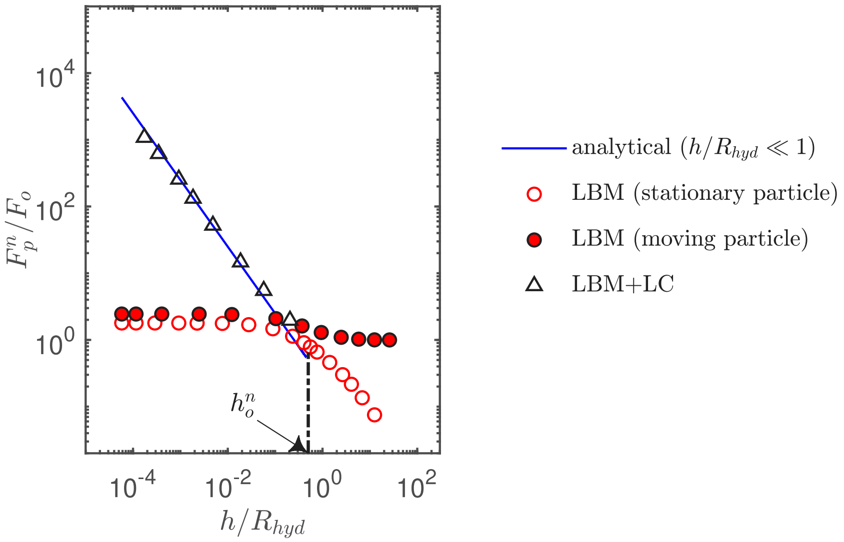

Fig. 11. The normal force on the stationary (open circles) and moving (filled circles) particle during a head-on collision of two spheres is compared for several dimensionless gaps. The forces are normalised by the Stokes drag force $F_o = 6\pi\mu u_p^x R_{hyd}$. $Re_p^t = 0.024$, and the dash–dot line shows the lubrication cutoff, $h_o^n/R_{hyd} = 0.5$. The open triangles indicate LBM simulation results with LC on the stationary particle.

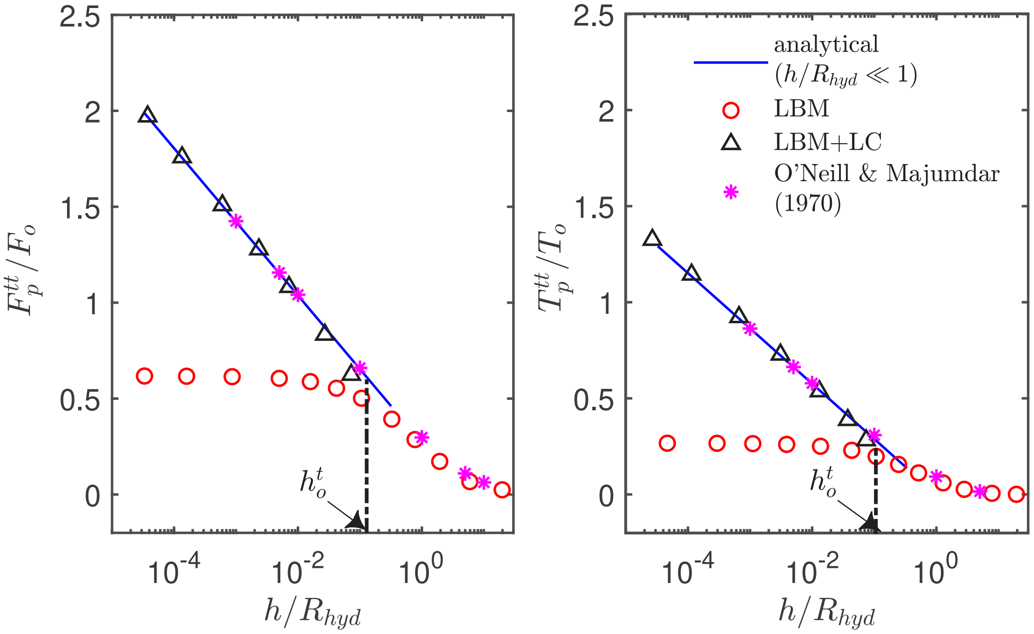

Fig. 12. The tangential forces (left) and torques (right) exerted on the stationary particle as evaluated by the LB simulation are compared against the analytical solution ($h \ll R_{hyd}$) and O'Neill and Majumdar (1970). $Re_p^t = 0.024$, and the dash–dot line indicates the normalised cutoff gap, $h_o^t/R_{hyd} = 0.1$ below which LC due to translation is applied.

Eq. (A.1a). Forces are normalised by the Stokes force $F_o = 6\pi\mu u_p^x R_{hyd}$. When the distances between the particles are large, the forces on the stationary and moving particles tend to be zero and one (Stokes value) respectively. However, as the distance decreases, the forces evaluated from the LB simulation approach a constant value ($\approx$2). Therefore, to measure the forces precisely over the small gaps, we turn on the LC when the distance between the particles is below the cutoff gap, $h_o^n = 0.5R_{hyd}$, when the LB-only simulation begins to separate from the analytical line. From the open triangles in Fig. 11, we can see that the LB simulation results with LC follow the analytical value.

A.2.2. Tangential effect of particle translation

Now we benchmark the tangential lubrication forces and torques due to translation of one particle relative to the second stationary particle. While the z position of the two particles was equal in the previous simulation (see Appendix A.2.1), here, the particle centres are off by a distance of one particle diameter along the z direction. The centre-centre distance along the x direction is $37.5R$ and the y positions of the spheres are equal. The particle is allowed to translate at a fixed speed in the positive x direction with $Re_p^t = 0.025$ and stopped when the surfaces touch. For gaps between $O(10\ lu)$ and $O(10^{-5}\ lu)$, we present in Fig. 12 (left panel), the comparison of the LB force (without LC) on the stationary particle with the analytical expression and with O'Neill and Majumdar (1970). Here, the tangential forces are normalised by $F_o = 6\pi\mu u_p^x R_{hyd}$. Since the stationary particle is far away from the translating particle, the forces approach zero in the limit of large h/R_{hyd}, and gradually saturate to $\approx$0.6 in short ranges. We determine the lubrication cutoff, h_o^t when the LB force equals the analytical value in the limit of small interparticle gaps. We can see from the left panel of Fig. 12 that the LB force stays constant below $h/R_{hyd} \approx 0.1$. Applying the

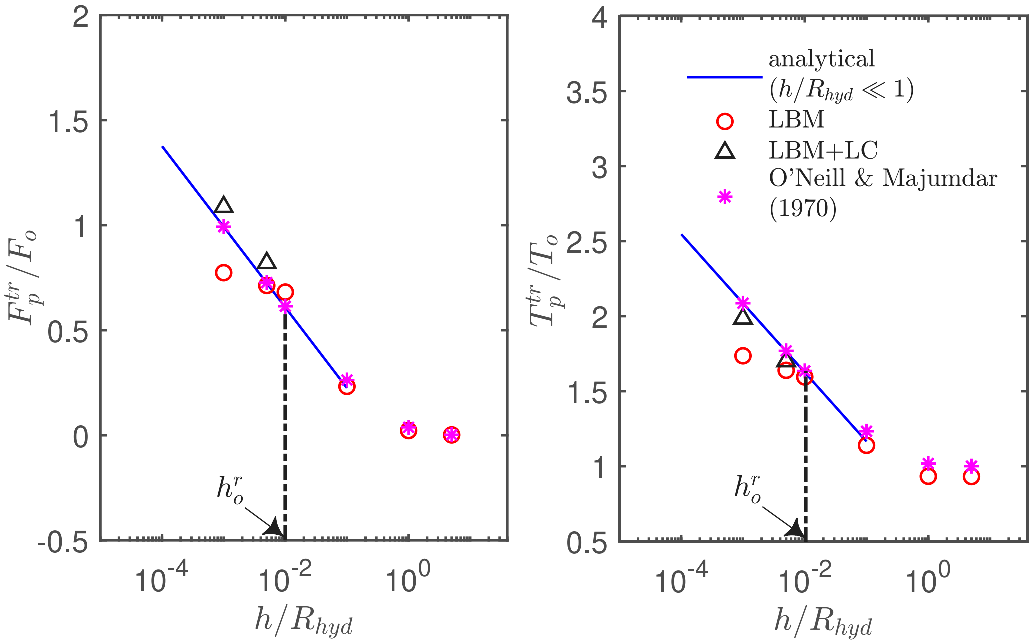

Fig. 13. The hydrodynamic forces (left) and torques (right) exerted on a rotating sphere computed from LBM simulation are compared with the previous results by O'Neill and Majumdar (1970), as well as the analytical expression. $Re_p^r = 0.22$, and the dash–dot line shows the cutoff gap, $h_o^r/R_{hyd} = 0.01$ below which LC due to rotation is applied.

lubrication correction (open triangles) results in an excellent agreement between our simulations, the analytical expression, and O'Neill and Majumdar (1970).

For the same simulation setup, the normalised tangential torques on the stationary particle for several gaps are presented in the right panel of Fig. 12. In long ranges, the tangential torques evaluate to zero and plateau to ≈0.3 in short ranges. With LC, our simulation results are consistent with the analytical equation and O'Neill and Majumdar (1970).

A.2.3. Tangential effect of particle rotation

For benchmarking the tangential forces and torques due to rotation, we consider several simulations in which the z positions between the stationary and rotating spheres vary between $5 \leq h/R_{hyd} \leq 0.001$. The x and y centres of mass of both particles are equal in all simulations. To ensure that steady-state is attained, all simulations was run up to 100,000 iterations with rotational particle Reynolds number $Re_p^r = \omega_p^y R_{hyd}^2/\nu = 0.22$. In the left panel of Fig. 13, we present the time-averaged hydrodynamic force on the rotating sphere normalised by $F_o = 6\pi\mu\omega_p^y R_{hyd}^2$ for several dimensionless gaps. The tangential cutoff due to rotation, h_o^r is determined when the time-averaged LB force (without LC) starts to separate from the analytical line. Up to $h/R_{hyd} = 0.01$, the simulation values agree well with O'Neill and Majumdar (1970), while the results plateau for small interparticle gaps. From the open triangles in the left panel of Fig. 13, it is evident that the corrected LB forces agree with the results in the literature.

In the right panel of Fig. 13, we present the time-averaged torques on the rotating particle normalised by the Stokes torque. The simulation parameters are the same as for the previous case. We can see that the torques start to plateau for small interparticle gaps. At sufficiently large gap widths, there is no interaction between the spheres and the torques on the particle are equal to the Stokes situation (≈1). All open triangles indicate the results of LB simulations with LC which agrees well with the analytical expression and with O'Neill and Majumdar (1970).

References

Andreotti, B., Barrat, J.L., Heussinger, C., 2012. Shear flow of non-Brownian suspensions close to jamming. Phys. Rev. Lett. 109 (10), 105901.

Berg, J.C., 2010. An Introduction to Interfaces & Colloids: The Bridge to Nanoscience. World Scientific.

Chaouche, M., Koch, D.L., 2001. Rheology of non-Brownian rigid fiber suspensions with adhesive contacts. J. Rheol. 45 (2), 369–382.

Chen, S., Doolen, G.D., 1998. Lattice Boltzmann method for fluid flows. Annu. Rev. Fluid Mech. 30 (1), 329–364.

Dbouk, T., Lobry, L., Lemaire, E., 2013. Normal stresses in concentrated non-Brownian suspensions. J. Fluid Mech. 715, 239–272.

Derksen, J.J., Sundaresan, S., 2007. Direct numerical simulations of dense suspensions: wave instabilities in liquid-fluidized beds. J. Fluid Mech. 587, 303–336.

Feng, Z.G., Michaelides, E.E., 2004. The immersed boundary-lattice Boltzmann method for solving fluid–particles interaction problems. J. Comput. Phys. 195 (2), 602–628.

Feng, Z.G., Michaelides, E.E., 2009. Robust treatment of no-slip boundary condition and velocity updating for the lattice-Boltzmann simulation of particulate flows. Comput. & Fluids 38 (2), 370–381.

Ferrari, L., Kaufmann, J., Winnefeld, F., Plank, J., 2011. Multi-method approach to study influence of superplasticizers on cement suspensions. Cem. Concr. Res. 41 (10), 1058–1066.

Gallier, S., Lemaire, E., Lobry, L., Peters, F., 2016. Effect of confinement in wall-bounded non-colloidal suspensions. J. Fluid Mech. 799, 100–127.

Hamed, S.B., Belhadri, M., 2009. Rheological properties of biopolymers drilling fluids. J. Pet. Sci. Eng. 67 (3–4), 84–90.

Hayakawa, H., 2020. Simulation of dense non-Brownian suspensions with the lattice Boltzmann method: shear jammed and fragile states. Soft Matter 16 (4), 945–959.

Hermes, M., Guy, B.M., Poon, W.C.K., Poy, G., Cates, M.E., Wyart, M., 2016. Unsteady flow and particle migration in dense, non-Brownian suspensions. J. Rheol. 60 (5), 905–916.

Hollander, E.D., Derksen, J.J., Bruinsma, O.S.L., Van den Akker, H.E.A., Van Rosmalen, G.M., 2001. A numerical study on the coupling of hydrodynamics and orthokinetic agglomeration. Chem. Eng. Sci. 56 (7), 2531–2541.

Karan, P., Chakraborty, J., Chakraborty, S., 2020. Influence of non-hydrodynamic forces on the elastic response of an ultra-thin soft coating under fluid-mediated dynamic loading. Phys. Fluids 32 (2), 022002.

Krieger, I.M., Dougherty, T.J., 1959. A mechanism for non-Newtonian flow in suspensions of rigid spheres. Trans. Soc. Rheol. 3 (1), 137–152.

Kromkamp, J., Van Den Ende, D., Kandhai, D., Van Der Sman, R., Boom, R.M., 2005. Shear-induced self-diffusion and microstructure in non-Brownian suspensions at non-zero Reynolds numbers. J. Fluid Mech. 529, 253.

Krüger, T., Kusumaatmaja, H., Kuzmin, A., Shardt, O., Silva, G., Viggen, E.M., 2017. The Lattice Boltzmann Method: Principles and Practice. Springer.

Krüger, T., Varnik, F., Raabe, D., 2011. Efficient and accurate simulations of deformable particles immersed in a fluid using a combined immersed boundary lattice Boltzmann finite element method. Comput. Math. Appl. 61 (12), 3485–3505.

Kumaran, V., 2009. Dynamics of dense sheared granular flows. Part 1. Structure and diffusion. J. Fluid Mech. 632, 109–144.

Ladd, A.J.C., 1994a. Numerical simulations of particulate suspensions via a discretized Boltzmann equation. Part 1. Theoretical foundation. J. Fluid Mech. 271, 285–309.

Ladd, A.J.C., 1994b. Numerical simulations of particulate suspensions via a discretized Boltzmann equation. Part 2. Numerical results. J. Fluid Mech. 271, 311–339.

Lattuada, E., Buzzaccaro, S., Piazza, R., 2016. Colloidal swarms can settle faster than isolated particles: enhanced sedimentation near phase separation. Phys. Rev. Lett. 116 (3), 038301.

Lin, N.Y.C., Guy, B.M., Hermes, M., Ness, C., Sun, J., Poon, W.C.K., Cohen, I., 2015. Hydrodynamic and contact contributions to continuous shear thickening in colloidal suspensions. Phys. Rev. Lett. 115 (22), 228304.

Liu, Y., Naidu, R., Ming, H., 2013. Surface electrochemical properties of red mud (bauxite residue): Zeta potential and surface charge density. J. Colloid Interface Sci. 394, 451–457.

Liu, J.Z., Wang, R.K., Gao, F.Y., Zhou, J.H., Cen, K.F., 2012. Rheology and thixotropic properties of slurry fuel prepared using municipal wastewater sludge and coal. Chem. Eng. Sci. 76, 1–8.

Mari, R., Seto, R., Morris, J.F., Denn, M.M., 2014. Shear thickening, frictionless and frictional rheologies in non-Brownian suspensions. J. Rheol. 58 (6), 1693–1724.

Masliyah, J.H., Bhattacharjee, S., 2006. Electrokinetic and Colloid Transport Phenomena. John Wiley & Sons.

McCullough, J.W.S., Aminossadati, S.M., Leonardi, C.R., et al., 2021. A 3D LBM-DEM study of sheared particle suspensions under the influence of temperature-dependent viscosity. Powder Technol. 390, 143–158.

Mitchell, T.R., Leonardi, C.R., 2016. Micromechanical investigation of fines liberation and transport during coal seam dewatering. J. Natl. Gas Sci. Eng. 35, 1101–1120.

Mumtaz, H.S., Hounslow, M.J., Seaton, N.A., Paterson, W.R., 1997. Orthokinetic aggregation during precipitation: A computational model for calcium oxalate monohydrate. Chem. Eng. Res. Des. 75 (2), 152–159.

Nguyen, N.-Q., Ladd, A.J.C., 2002. Lubrication corrections for lattice-Boltzmann simulations of particle suspensions. Phys. Rev. E 66 (4), 046708.

O'Neill, M.E., Majumdar, R., 1970. Asymmetrical slow viscous fluid motions caused by the translation or rotation of two spheres. Part 1. The determination of exact solutions for any values of the ratio of radii and separation parameters. Z. Angew. Math. Phys. ZAMP 21 (2), 164–179.

Pednekar, S., Chun, J., Morris, J.F., 2017. Simulation of shear thickening in attractive colloidal suspensions. Soft Matter 13 (9), 1773–1779.

Perkins, E., Williams, J.R., 2002. Generalized spatial binning of bodies of different sizes. In: Discrete Element Methods: Numerical Modeling of Discontinua. pp. 52–55.

Rohde, M., Derksen, J.J., Van den Akker, H.E.A., 2002. Volumetric method for calculating the flow around moving objects in lattice-Boltzmann schemes. Phys. Rev. E 65 (5), 056701.

Rouyer, F., Lhuillier, D., Martin, J., Salin, D., 2000. Structure, density, and velocity fluctuations in quasi-two-dimensional non-Brownian suspensions of spheres. Phys. Fluids 12 (5), 958–963.

Sarkar, S., Shatoff, E., Ramola, K., Mari, R., Morris, J.F., Chakraborty, B., 2017. Shear-induced organization of forces in dense suspensions: signatures of discontinuous shear thickening. In: EPJ Web of Conferences, Vol. 140. EDP Sciences, p. 09045.

Shan, X., Chen, H., 1993. Lattice Boltzmann model for simulating flows with multiple phases and components. Phys. Rev. E 47 (3), 1815.

Sierou, A., Brady, J.F., 2002. Rheology and microstructure in concentrated noncolloidal suspensions. J. Rheol. 46 (5), 1031–1056.

Silaghi, F.A., Giunchi, A., Fabbri, A., Ragni, L., 2010. Estimation of rheological properties of gelato by FT-NIR spectroscopy. Food Res. Int. 43 (6), 1624–1628.

Simeonov, J.A., Calantoni, J., 2012. Modeling mechanical contact and lubrication in direct numerical simulations of colliding particles. Int. J. Multiph. Flow. 46, 38–53.

Srinivasan, S., Van den Akker, H.E.A., Shardt, O., 2020a. Shear thickening and history-dependent rheology of monodisperse suspensions with finite inertia via an immersed boundary lattice Boltzmann method. Int. J. Multiph. Flow. 103205.

Srinivasan, S., Van den Akker, H.E., Shardt, O., 2021. Numerical simulations of dense granular suspensions in laminar flow under constant and varying shear rates. Comput. & Fluids 105115.

Ten Cate, A., Nieuwstad, C.H., Derksen, J.J., Van den Akker, H.E.A., 2002. Particle imaging velocimetry experiments and lattice-Boltzmann simulations on a single sphere settling under gravity. Phys. Fluids 14 (11), 4012–4025.

Thorimbert, Y., Marson, F., Parmigiani, A., Chopard, B., Lätt, J., 2018. Lattice Boltzmann simulation of dense rigid spherical particle suspensions using immersed boundary method. Comput. & Fluids 166, 286–294.

Toll, S., Månson, J.-A.E., 1994. Dynamics of a planar concentrated fiber suspension with non-hydrodynamic interaction. J. Rheol. 38 (4), 985–997.

Vázquez-Quesada, A., Mahmud, A., Dai, S., Ellero, M., Tanner, R.I., 2017. Investigating the causes of shear-thinning in non-colloidal suspensions: Experiments and simulations. J. Non-Newton. Fluid Mech. 248, 1–7.

Van de Ven, T.G.M., 1982. Interactions between colloidal particles in simple shear flow. Adv. Colloid Interface Sci. 17 (1), 105–127.

Vowinckel, B., Withers, J., Luzzatto-Fegiz, P., Meiburg, E., 2019. Settling of cohesive sediment: particle-resolved simulations. J. Fluid Mech. 858, 5–44.

Wang, G., Wan, D., Peng, C., Liu, K., Wang, L.-P., 2019. LBM Study of aggregation of monosized spherical particles in homogeneous isotropic turbulence. Chem. Eng. Sci. 201, 201–211.

Williams, J.R., Perkins, E., Cook, B., 2004. A contact algorithm for partitioning n arbitrary sized objects. Eng. Comput..

Yeo, K., Maxey, M.R., 2010. Ordering transition of non-Brownian suspensions in confined steady shear flow. Phys. Rev. E 81 (5), 051502.